nature neuroscience

Article

https://doi.org/10.1038/s41593-024-01683-7

Medial entorhinal cortex mediates learning of context-dependent interval timing behavior

Received: 24 March 2023

Accepted: 14 May 2024

Published online: 14 June 2024

Check for updates

Erin R. Bigus[1,3], Hyun-Woo Lee[2,3], John C. Bowler[2], Jiani Shi[2] & James G. Heys[2]

Episodic memory requires encoding the temporal structure of experience and relies on brain circuits in the medial temporal lobe, including the medial entorhinal cortex (MEC). Recent studies have identified MEC 'time cells', which fire at specific moments during interval timing tasks, collectively tiling the entire timing period. It has been hypothesized that MEC time cells could provide temporal information necessary for episodic memories, yet it remains unknown whether they display learning dynamics required for encoding different temporal contexts. To explore this, we developed a new behavioral paradigm requiring mice to distinguish temporal contexts. Combined with methods for cellular resolution calcium imaging, we found that MEC time cells display context-dependent neural activity that emerges with task learning. Through chemogenetic inactivation we found that MEC activity is necessary for learning of context-dependent interval timing behavior. Finally, we found evidence of a common circuit mechanism that could drive sequential activity of both time cells and spatially selective neurons in MEC. Our work suggests that the clock-like firing of MEC time cells can be modulated by learning, allowing the tracking of various temporal structures that emerge through experience.

Our daily experiences unfold across space and time, meaning that the brain must capture these dimensions to accurately form episodic memories (that is, memories of personal experiences that occur in a specific spatial and temporal context)[1,2]. Medial temporal lobe (MTL) structures are critical for episodic memory, raising the question of how these regions encode space and time. A remarkable series of findings have revealed the role of MTL structures in encoding space, beginning with the findings that: (1) MTL regions are critical in memory-guided spatial navigation behavior[3–6]; (2) MTL regions contain so-called place cells in the hippocampus[5,7] and grid cells in the MEC[8] that fire when animals visit particular locations within an environment; and (3), critically, spatial cells remap, reorganizing their firing fields as animals navigate and learn features of different environments to form a unique map for each spatial context[9,10]. Observing such learning dynamics provided the invaluable insight that a key role of spatially tuned cells is likely to create a 'cognitive map' of an environment[11,12] that can be stored in memory and used to guide future behavior.

In contrast to spatial context, it remains relatively unknown how temporal context, or the temporal structure of experiences, is encoded within the MTL memory system. The nervous system must track time across many scales, ranging from milliseconds to hours, but the intermediate scale of interval timing (seconds to minutes) is perhaps most relevant for planning and executing daily behaviors, including foraging, mating, prey capture and avoidance[13–15]. Accordingly, encoding the temporal structure of daily experiences requires interval timing. Although it is largely unclear how the passage of interval time and

[1]Interdepartmental PhD Program in Neuroscience, University of Utah, Salt Lake City, UT, USA. [2]Department of Neurobiology, University of Utah, Salt Lake City, UT, USA. [3]These authors contributed equally: Erin R. Bigus, Hyun-Woo Lee. e-mail: jim.heys@neuro.utah.edu

https://doi.org/10.1038/s41593-024-01683-7

the duration of events are tracked and recorded within the MTL, one intriguing possibility is that common mechanisms support encoding of both space and time[16]. If so, as for space, we would expect MTL regions to: (1) be necessary for interval timing behavior; (2) contain cells selective to time; and (3) use distinct patterns of time-selective cells to form 'timelines' of unique experiences, akin to maps. Previous work suggests that MEC fits the first two criteria: MEC is necessary for interval timing behavior[17–19] and contains time cells that fire regularly at discrete moments as rodents report temporal durations on the scale of seconds[20]. As a population, different MEC time cells fire regularly at different moments in a timed interval, like the second hand of a clock, thereby forming a sequence of neural activity, tiling the entire timing epoch. Third, by analogy to spatial cells, MEC time cells could play a key role in episodic memory by using unique time cell trajectories to form distinct 'maps' or 'timelines' of temporal experiences (that is, contexts). The third point makes clear predictions about the learning dynamics of MEC time cells: distinct patterns of time cells should emerge as animals learn the temporal structure of an experience, and emergence of these patterns should be necessary for timing behavior. Evidence of such learning dynamics could suggest that MEC time cells play a key role in the formation of episodic memories by encoding the temporal structure of experiences. However, these predictions have yet to be experimentally tested.

We therefore aimed to test the hypotheses that (1) distinct sequences of time cells will become active as animals learn to identify a new temporal context, forming a unique map or 'timeline' of each temporal context, and (2) such dynamics support learning of timing behavior. To address these questions, we developed a new temporal delayed nonmatch to sample (tDNMS) task that requires mice to differentiate the temporal structure of trials (temporal context). By performing two-photon calcium imaging as mice performed the tDNMS task, we uncovered populations of MEC time cells that fire selectively at specific moments in the timing task, with the population of time cells creating a sequence that spans the entire timing epoch. Remarkably, we find that, over the course of learning, these sequences become context dependent, whereby MEC time cells become differentially active on particular trial types. Furthermore, multiple lines of evidence suggest that the activity of MEC time cells plays a causal role specifically in learning context-dependent interval timing behavior. Finally, we find evidence for a common circuit mechanism that may support both MEC spatial and time coding. Our results suggest that MEC time cells may play a central role in episodic memory by forming unique 'timelines' that encode the temporal structure of distinct experiences.

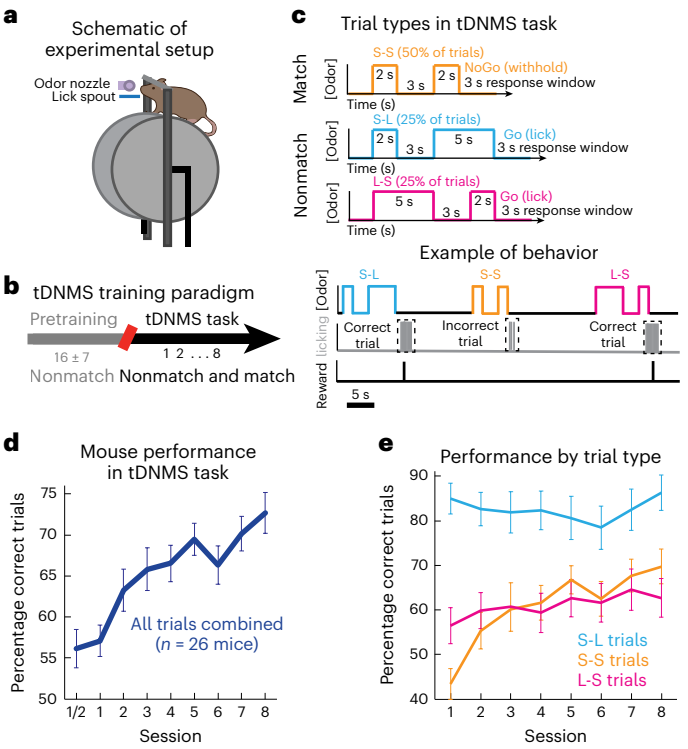

Fig. 1 | Mice learn new tDNMS task. a, Simplified experimental setup. **b**, Overview of training paradigm. Mice were first pretrained to lick at the offset of nonmatch trials to trigger reward delivery. On reaching criteria after an average of 16 sessions (mean ± s.d.), mice began 8 training sessions on the tDNMS task, where match trials were introduced. **c**, Trial types and example behavior. The tDNMS task consisted of three types of trials defined by stimulus durations: S-S, S-L and L-S. To perform the task correctly, mice must lick in the response window after nonmatch trials and withhold licking in match trials. **d**, Percentage correct across all trial types for each session, averaged across all mice (mean ± s.e.m., $n = 26$ mice). **e**, Percentage correct by trial type for each session, averaged across all mice (mean ± s.e.m., $n = 26$ mice).

Results

Mice learn new tDNMS task using flexible timing behavior

We designed a timing task with two objectives. First, mice must track time and make decisions based on the temporal structure of each trial. In addition, the task should require cognitive flexibility to maximally engage the MTL memory system. This second point may be critical to elicit learning dynamics, considering that learning flexible but not rigid navigation behavior requires the MTL[21]. To meet these two goals, we adapted the delayed nonmatch to sample (DNMS) task structure, known to engage the MTL[22–24], to create a new tDNMS task. As mice heavily rely on olfaction, we built a flow dilution olfactometer (Extended Data Fig. 1a)[25] and signaled stimuli via a single odorant (isoamyl acetate). We validated our system by ensuring that the concentration of the odorant remained constant over the course of a full training session and that odor concentration could be rapidly controlled (Extended Data Fig. 1b).

In each trial of the tDNMS task, a water-restricted, head-fixed mouse (Fig. 1a) was presented with two successive stimuli for either a short (2 s) or a long (5 s) duration, separated by a brief 3-s interstimulus interval (ISI). Trials were performed in the dark and separated using (1) a 16- to 24-s intertrial interval (ITI) and (2) a light pulse (0.25 s) to signal the start of the trial (Extended Data Fig. 1c). The tDNMS task consisted of three trial types defined by each stimulus duration: short–long (S-L), long–short (L-S) and short–short (S-S). Using a 'Go–NoGo' strategy, mice were trained to lick to report a nonmatch of durations (Go trials; S-L and L-S) and withhold from licking in response to match durations (NoGo trials; S-S) (Fig. 1c).

Before starting the tDNMS task, mice underwent a shaping procedure to learn the trial structure. Mice were presented only with nonmatch trials and learned to refrain from licking during the first odor and ISI, then licked near the second odor offset to earn a reward (Fig. 1b and Extended Data Fig. 1d). After mice reached criteria (Methods), indicating learning of the 'odor, odor, response' trial structure, mice started the tDNMS task, where match trials were first introduced and equally balanced with nonmatch trials over each session (90 trials per session over ~45 min). Notably, although mice could employ a simple strategy of licking after the second odor offset during pretraining, the introduction of match trials transformed the task into one that required timing.

To test whether mice learn the tDNMS task, we monitored behavioral performance in 26 mice over 8 training sessions (Fig. 1d). Although mice began at chance performance, they steadily improved with training, averaging 72.7 ± 2.5% (mean ± s.e.m. for all data unless otherwise reported) correct responses on session 8, demonstrating learning (27.1 ± 4.1% change from session 1 to sessions 7 and 8; repeated-measures analysis of variance (ANOVA) $F_{7,25} = 8.43$, $P < 0.001$). To better understand the learning process, we examined performance by trial type. We expected mice to begin the task by licking at the second

odor offset, given their pretraining, and thus perform well in nonmatch trials. Indeed, mice averaged 85.3 ± 3.5% correct S-L trials on day 1 of the tDNMS task, compared with 91.1 ± 2.7% on the last half-session of pretraining (Fig. 1e and Extended Data Fig. 1g; Student's paired *t*-test, $P = 0.24$). Unexpectedly, performance on L-S trials dropped from 86.3 ± 2.0% correct responses on the last half-session of shaping to 56.6 ± 4.1% correct on day 1 of the task (Fig. 1e and Extended Data Fig. 1g; Student's paired *t*-test, $P < 0.001$). Mice could miss nonmatch trials either by incorrectly withholding licking or by licking prematurely. Most mistakes were from premature licking, suggesting that mice reverted to an impulsive action of licking after long odors previously observed in shaping (Extended Data Fig. 1h–i). Match trials uniquely require learning a new response of withholding, so we expected learning to occur here. Indeed, mice began with poor performance, averaging 43.4 ± 3.5% correct S-S trials on day 1 owing to their tendency to lick near the second odor offset (Extended Data Fig. 1j), as if applying an 'odor, odor, lick' strategy learned in pretraining. However, by day 8, mice learned to withhold licking, reaching 70 ± 4% correct S-S trials (repeated-measures ANOVA $F_{7,25} = 4.81$, $P < 0.001$). Together, our data demonstrated that mice learned the tDNMS task by learning to withhold licking selectively on S-S trials, as evidenced by (1) improvement on S-S trials, (2) high performance on S-L trials and (3) a tendency to miss L-S trials by licking early.

Limiting the task to three trial types allowed mice to robustly learn the tDNMS task over seven to eight sessions. However, this task design could inadvertently lead mice to adopt a rigid cognitive strategy. For instance, mice could distinguish trials based on their total duration, circumventing the need to assess the durations of individual stimuli. We conducted two control experiments to test this possibility. First, we performed experiments without odor to establish that olfactory cues are essential for task engagement (Extended Data Fig. 1e). Then, we trained a cohort of mice on a modified version of the tDNMS task and manipulated the ISI in a subset of probe trials to make nonmatch and match trials the same duration. Performance was unaffected, demonstrating that mice respond to individual stimuli and not the overall length of the trial (Extended Data Fig. 1f). Importantly, our results did not confirm that mice compared durations; mice probably use a simpler strategy (discussed later). Nevertheless, any strategy required them to (1) monitor stimuli durations and (2) make decisions based on the stimuli's position within the trial structure. Therefore, the tDNMS task met our goals of requiring mice to make flexible decisions based on the temporal structure of each trial.

MEC time cells fire in context-dependent trajectories

To characterize the learning dynamics of MEC time cells, we applied methods that we have previously developed for large-scale, cellular resolution, two-photon calcium imaging in MEC[20,26] (Fig. 2a,b). We recorded from populations of layer II MEC neurons expressing GCaMP6s (Fig. 2c-e and Extended Data Fig. 2a), across six mice (field of view (FOV) 430 ± 54 µm medial to lateral by 380 ± 45 µm dorsal to ventral; depth below the surface 105 ± 8 µm) as well-trained mice performed the tDNMS task (15 ± 4 d pretraining then 13 ± 8 d of tDNMS training to reach day *N*; 82 ± 5% correct trial performance). Across the total population (2,056 active neurons), we found that 33.8% of cells exhibited regular time-locked activity at a particular moment in each trial (Fig. 2f and Extended Data Fig. 2b). Consistent with previous reports during interval timing behavior[20], we found that different MEC 'time cells' were selectively active at different delay times from the start of each trial, forming a regular temporal sequence that spanned the entire trial epoch (Fig. 2g and Extended Data Fig. 3a).

During the tDNMS task, mice were free to run on a cylindrical treadmill. As previous work has shown that MEC neurons can encode distance traveled[27,28], we wondered whether the time-locked activity of MEC time cells might be better explained by distance traveled from trial onset. In support of the idea that MEC time cells encode elapsed time in the task, and not distance traveled, we found that the vast majority of time cells displayed a smaller coefficient of variation (CV) when measuring as a function of elapsed time versus distance traveled from trial onset (CV of elapsed time: 48.4 ± 0.8, elapsed distance: 205.7 ± 4.4, $P < 0.0001$, $t_{(1,070)} = 39.9$, paired Student's *t*-test; Fig. 2h). In addition, to estimate the specific contribution of different behavioral variables (distance traveled (*D*), time elapsed (*T*) and licking (*L*)) on the activity of MEC neurons, we used a generalized linear model (GLM) to fit calcium activity (d*F*/*F*) as a Gaussian linear function of different combinations of the three behavioral variables[29,30]. Consistent with results using the CV, our GLM results show that the log-likelihood gained by time is significantly greater than the log-likelihood gained by either distance or licking (Extended Data Fig. 3b–d), indicating that cells are tuned to elapsed time in the tDNMS task.

To perform the tDNMS task, subjects must perceive and use stimuli durations to determine trial type (that is, nonmatch or match) and learn the appropriate response (that is, Go or NoGo, respectively). Importantly, as trials consist of unique sequences of cues (differing only in duration) that dictate the appropriate behavioral response, we refer to each trial type as a temporal context. The robust learning and task structure allowed us to ask whether differential activity of populations of time cells encode each trial type, or temporal context. Although some time cells showed stable activity across trial types (time cell 1 in Fig. 2f), others displayed activity specific to the temporal context. This context-dependent activity took various forms. By examining time field stability across each pair of trial types (S-S versus S-L, S-S versus L-S, S-L versus L-S; Extended Data Fig. 3e), we found that more than half of the time cells exhibited stable time fields (58.4%, $n = 944$ out of 1,617). For those that 'remapped' between contexts, time fields usually either disappeared in one trial type (time cells 3–5 in Fig. 2f; 33.2%, $n = 537$ of 1,617) or modulated their firing rate (time cell 6 in Fig. 2f; 5.32%, $n = 86$ of 1,617). Few time cells shifted the timing of peak activity (time cell 2 in Fig. 2f; 3.09%, $n = 50$ of 1,617). Together, these results demonstrated that time cell activity varies dynamically across temporal contexts, forming a unique trajectory or 'timeline' for each trial type.

Context-dependent sequences support tDNMS learning

Initially, on day 1, mice do not utilize temporal context to guide behavior; however, over several training sessions, they learn to respond correctly on 70–90% of trials per session. If context-dependent MEC time cell activity supports task learning, our data should support several predictions. First, context-dependent activity should be relatively absent on day 1 and emerge over the course of learning. Second, the coherence of individual time cell activity and/or the regular sequential neural activation across the population should be disrupted on 'error trials', when mice incorrectly report match or nonmatch.

To test the first prediction, we averaged the activity of MEC time cells for each trial type and compared the correlations for each cell's response across trial types, before and after learning (Methods). As mice learn at varying rates, we classify post-learning sessions with >70% correct trials as 'day *N*' (training session nos. 4–21). We found that the average correlation of time cell rate maps across match and nonmatch trials was significantly lower on day *N* compared with day 1 (day 1: 0.57 ± 0.01; day *N*: 0.42 ± 0.02; $P < 0.0001$, $z = 6.8$, Wilcoxon's rank-sum test; Fig. 3a-c), demonstrating that context-dependent activity develops to become more distinct over the course of learning.

The information required to distinguish contexts accumulates throughout each trial, with key moments providing enough information for an 'ideal observer' to discern the trial context. We wondered whether the population dynamics of context-dependent MEC time cells might be informative about this time-dependent decision process and further link neural dynamics to task learning. To test this, we measured the difference in d*F*/*F* for each time cell across trial types at successive moments in the trial epoch and averaged across time cells to generate population vectors. We found that the neural dynamics

https://doi.org/10.1038/s41593-024-01683-7

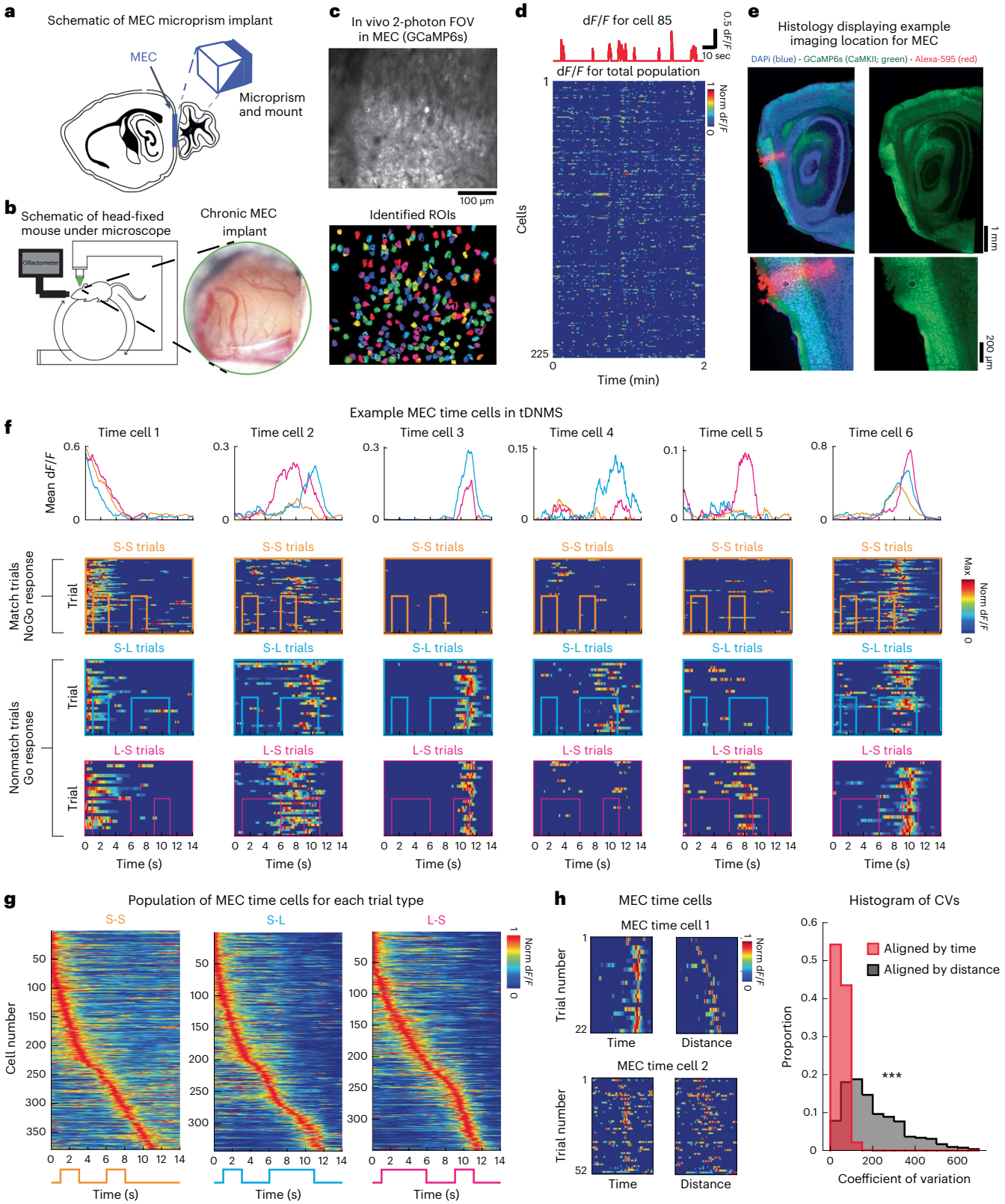

Fig. 2 | MEC time cells exhibit context-dependent sequential neural activity. a, Optical approach for imaging in MEC. **b,** Left, mouse positioned on the cylindrical treadmill and underneath the two-photon microscope. The olfactometer delivers odor near the mouse snout. Right, image of MEC prep following chronic implant. **c**, Average image of example FOV labeled with GCaMP6s (top) and ROIs from this FOV (below) ($n = 6$ mice). **d**, Example dF/F time series for individual neurons (top) and all ROIs from **c** (below). **e**, Representative histology. The red pin mark indicates relative location of the imaging field ($n = 6$ mice). **f**, Example individual MEC time cells. MEC time cell 1 is stable across all trial types (that is, context independent). MEC time cells 2–6 are significantly differentially active across specific trial types (that is, context dependent). **g**, All MEC time cells sorted for each trial type. **h**, Left, example time cells plotted as a function of elapsed time and distance traveled from trial onset. Right, distribution of CV for all MEC time cells, measured as a function of elapsed time and distance traveled from the trial onset ($t_{(1,070)} = 39.9, P = 2.7 \times 10^{-214}, n = 1{,}071$, two-sided, paired Student's t-test).

significantly diverge from a null distribution (with randomly assigned trial labels) at key moments after the stimuli have become distinct across contexts (Fig. 3d). For instance, the long stimuli on L-S trials could be used to classify L-S trials earlier in the trial epoch than the other trial types. Accordingly, neural dynamics diverged from the null distribution earlier when comparing L-S with S-S versus S-L with S-S trials (Fig. 3d). Importantly, we found that, over learning, these differences became more pronounced (discriminant index for S-S versus S-L: day 1 = 0.40 ± 0.07, day *N* = 0.67 ± 0.08, $P = 0.01$, $z = 2.55$; S-S versus L-S: day 1 = 0.52 ± 0.07, day *N* = 1.00 ± 0.09, $P < 0.001$, $z = 3.80$, Wilcoxon's rank-sum test; Extended Data Fig. 3g). Using a separate measure to assess learning, we also found that, from day 1 to day *N*, the population of MEC time cells shifts on each trial type to encode later times in the trial, which correspond to moments when there is sufficient information to disambiguate the trial type (peak times on day 1: 3.66 ± 0.17 s, day *N*: 4.67 ± 0.18 s, $P < 0.0001$, $z = 4.70$, Wilcoxon's rank-sum test; early peak proportion on day 1: 36% ($n = 164$ of 450), day *N*: 19% ($n = 76$ of 402), $P < 0.0001$, $\chi^2_{(1)} = 30.4$, χ^2 test; Fig. 3e,f).

Next, we asked whether the ensemble activity of time cells on individual trials contains enough information to accurately decode the temporal context. During the late phase of trials (9–11 s), ensemble activity exhibited distinct separation according to trial type as shown by linear discriminant analysis (LDA) (Fig. 3g and Extended Data Fig. 4a). To quantify this separation, we applied *k*-means clustering to each animal's LDA plot, revealing a clustering accuracy substantially higher than the bootstrapped chance level in five out of six animals (for mice 1–6: $P = 0$, 0.04, 0.08, 0, 0 and 0.001, respectively). This result was corroborated using an alternative classification method: we constructed a model using a support vector machine (SVM) to classify trials by type or as match versus nonmatch (Fig. 3h). As expected, when the model was trained and tested using neural activity during the early phase of trials (0–2 s), it failed to correctly identify trial information (trial type decoding for mice 1–6: all *P* values >0.1; match versus nonmatch decoding for mice 1–6: all *P* values >0.1). In contrast, when utilizing activity during the late phase (9–11 s), the model successfully decoded trial identity in most animals (trial type decoding for mice 1–6: *P* value = 0, 0.002, 0.25, 0, 0 and 0; match versus nonmatch decoding for mice 1–6: *P* value = 0, 0, 0.05, 0, 0 and 0), aligning with findings from the *k*-means clustering analysis. Together, these results support prediction 1 showing that context-dependent MEC time cell activity emerges over learning, eventually displaying an over-representation at later moments in the task, with large deviations in context-dependent neural trajectories near key moments in the task when it is possible to distinguish trial type.

To test our second prediction, we compared the average response for each MEC time cell for correct and error trials. The results show significantly higher coherence for time cells across randomly selected blocks of correct trials compared with error trials on day *N* (correlation between correct trials – group A and correct trials – group B: 0.51 ± 0.01 correct trials – group A and error trials: 0.26 ± 0.03, $P < 0.0001$, $z = 7.5$, Wilcoxon's signed-rank test; Fig. 3i,j). Furthermore, when comparing correct versus error trials on day 1 and day *N*, we found that the average correlation on day *N* was significantly reduced compared with day 1 (session type main effect: $P < 0.0001$, $F_{(1, 288)} = 18.5$; trial-type main effect: $P = 0.12$, $F_{(1.93, 555.15)} = 2.1$; interaction: $P = 0.33$, $F_{(1.93, 555.15)} = 1.1$, two-way mixed ANOVA with trial type and session factors; Extended Data Fig. 4b–e), providing additional support that MEC time cell dynamics evolve over learning. Together, our results demonstrating (1) the emergence of context-dependent time cell activity over learning and (2) altered coding during error trials support the hypothesis that MEC time cells form unique trajectories used to encode the structure of each trial type and likely used to guide context-dependent timing behavior.

Do time cells flexibly adapt to changes in task structure?

The presence of context-dependent dynamics suggests that MEC time cells reflect the temporal structure of a trial. To expand on this finding, we asked how time cells would adjust to manipulations in trial structure. In a subsequent session, we ran the normal tDNMS task, then halfway through the session introduced a lengthened ISI of 5 s (Extended Data Fig. 5a). Mice responded to the change in the ISI by delaying approach behavior and predictive licking, indicating perception of the changed trial structure (Extended Data Fig. 5b). On average, population-level MEC time cell activity was delayed in response to the longer ISI (peak times on normal and probe trials: S-S trial types: normal (6.3 ± 0.4 s) versus probe (7.8 ± 0.5 s), $P < 0.0001$ $z = 3.9$; S-L trial types: normal (4.3 ± 0.5 s) versus probe (6.2 ± 0.6 s), $P < 0.0001$, $z = 4.5$; L-S trial types: normal (5.1 ± 0.6 s) versus probe (7.5 ± 0.6 s), $P < 0.0001$, $z = 4.2$; Wilcoxon's signed-rank test; Extended Data Fig. 5c,d), further demonstrating that MEC time cells flexibly adapt to trial structure.

MEC is required to learn context-dependent timing behavior

The emergence of context-dependent MEC time cells provides a potential neural dynamical mechanism that could underlie tDNMS learning, where the formation of context-dependent 'timelines' (that is, time cell trajectories) could allow animals to differentiate trial types. To causally test whether MEC activity is necessary to learn the tDNMS task, we used a chemogenetic approach to inhibit MEC (Fig. 4a and Extended Data Fig. 6a,b). First, we bilaterally injected adeno-associated virus (AAV) expressing the inhibitory designer receptors exclusively activated by designer drug (DREADD) hM4D across the dorsal–ventral extent of MEC (Fig. 4b and Extended Data Fig. 8). Mice then underwent water restriction and shaping before starting the tDNMS task. We monitored learning across eight sessions of the tDNMS task, administering the DREADD agonist deschloroclozapine (DCZ) intraperitoneally (i.p.) 5 min before each session to inhibit MEC for the duration of training. As expected, control mice learned the task within 8 d, averaging 72.8 ± 2.6% correct responses across sessions 7 and 8 (Fig. 4c) (repeated-measures ANOVA $F_{7,15} = 5.09$, $P < 0.001$). In contrast, DREADD mice showed no improvement from session 1

Fig. 3 | Context-dependent MEC time cell population dynamics support learning of flexible interval timing behavior. a, Top, the population of MEC time cells significantly tuned to S-S trials and sorted by response times during S-S trials, depicted for S-S (left), S-L (middle) and L-S (right) trials on day 1. Bottom, same as top, but for day *N* sessions. **b**, Top two principal components (PCs) displayed for population of MEC time cells across trial types. **c**, Mean Pearson's correlation coefficients of MEC time cells across different trial types for day 1 (black) and day *N* (green) (day 1, $n = 449$, day *N*, $n = 452$, $z = 6.8$, $p = 1.3 \times 10^{-11}$, two-sided Wilcoxon's rank-sum test). **d**, Left, population vector for the difference in d*F*/*F* computed for each MEC time cell across S-S and S-L trial types as a function of trial time. Solid lines are the actual data and shades indicate 0.1th and 99.9th percentiles of shuffle data. Right, the same for S-S versus L-S trials. **e**, Sorted sequence of MEC time cells in L-S trials on day 1 (left) and day *N* (right). **f**, Histogram of the timing of peak responses for all MEC time cells on day 1 (black) and day *N* (green), for all three trial types (day 1, $n = 450$, day *N*, $n = 402$, $z = 4.70$, $P = 2.7 \times 10^{-6}$, two-sided Wilcoxon's rank-sum test). **g**, A representative LDA plot for individual trials. **h**, Decoding accuracy of SVM models for trial types (left) or match versus nonmatch (right). The models are built on neural activity from either early phase or late phase trials. Color circles depict the accuracy from actual data, with oval shades representing 2.5th and 97.5th percentiles of shuffle data. Each color corresponds to an individual animal ($n = 6$; trial type decoding in early: $z = 0.03$, $P = 0.97$; in late: $z = 4.16$, $P = 3.1 \times 10^{-5}$; match versus nonmatch decoding in early: $z = 0.66$, $P = 0.51$; in late: $z = 4.20$, $P = 2.6 \times 10^{-5}$, two-sided Wilcoxon's rank-sum test). **i**, MEC time cells during S-S correct trials A (left; sorted by A), correct trials B (middle; sorted by A) and S-S error trials (right; sorted by A) on day *N* of training in the tDNMS task. **j**, Cumulative distribution for Pearson's correlation coefficients calculated for MEC time cells comparing correct trials A with B (blue), and correct trials A with error trials (red) (Methods) (day 1, $n = 120$, day *N*, $n = 170$, $z = 7.5$, $P = 8.5 \times 10^{-14}$, two-sided Wilcoxon's signed-rank test).

https://doi.org/10.1038/s41593-024-01683-7

(57.2 ± 2.6% correct responses) to sessions 7 and 8 (59.1 ± 3.3% correct responses) (repeated-measures ANOVA $F_{7,14} = 1.18$, $P = 0.32$). Inactivation of MEC prevented mice from learning the tDNMS task.

To investigate the specific deficit caused by MEC inhibition, we analyzed data by trial type. Both control and DREADD mice performed well on S-L trials, starting immediately on session 1 (Fig. 4e), as a result of learning that took place during the shaping phase of the task (before DCZ injections) (Extended Data Fig. 6d). In contrast, on day 1 both control and DREADD mice exhibited poor performance on L-S nonmatch trials, seemingly as a result of impulsive tendencies causing them to lick after the long odor presentation, a behavior noted during the shaping phase (Extended Data Fig. 6e-f). As match trials uniquely demand the learning of a new withholding response, we anticipated that improvement in these trials would drive overall

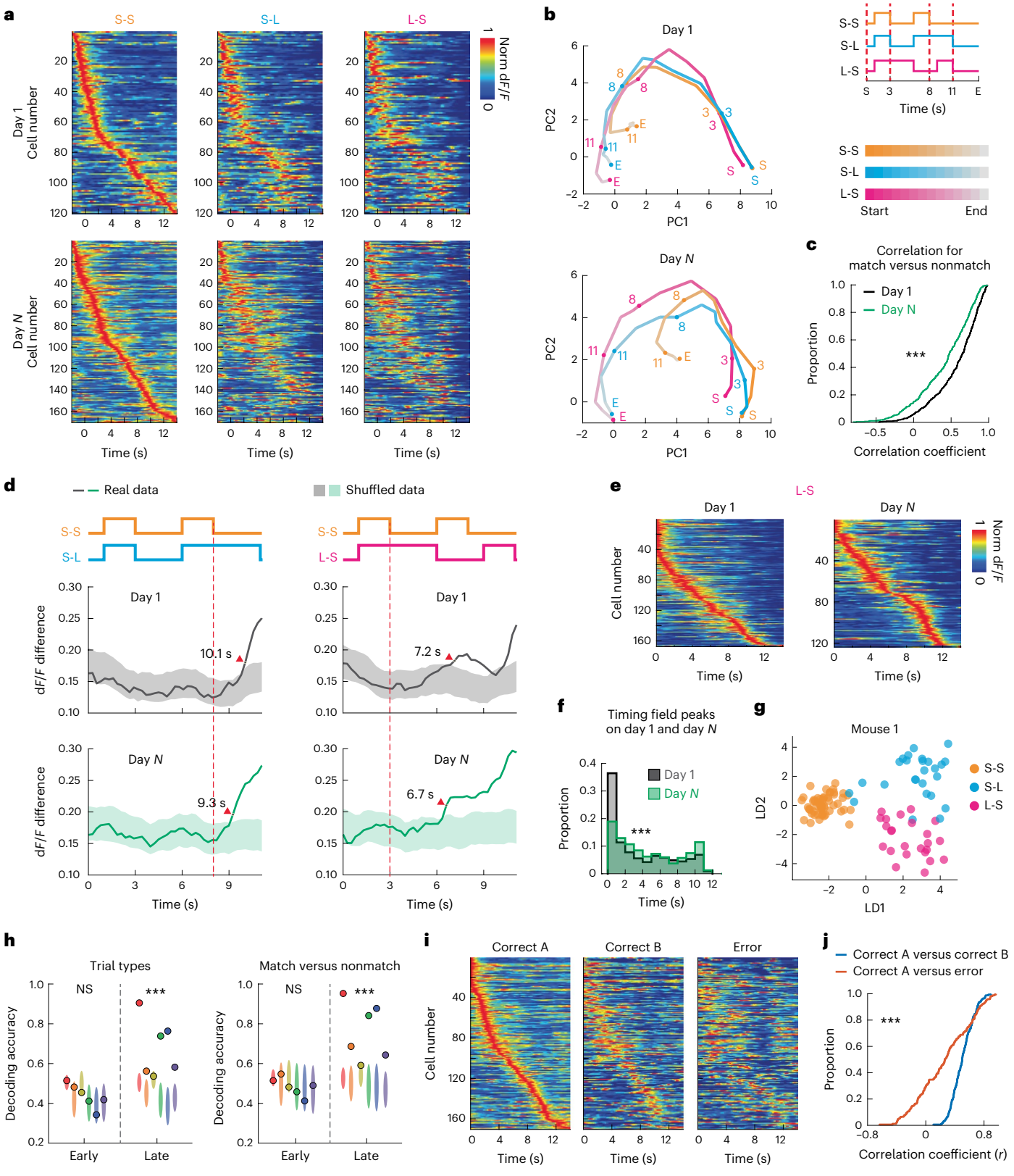

https://doi.org/10.1038/s41593-024-01683-7

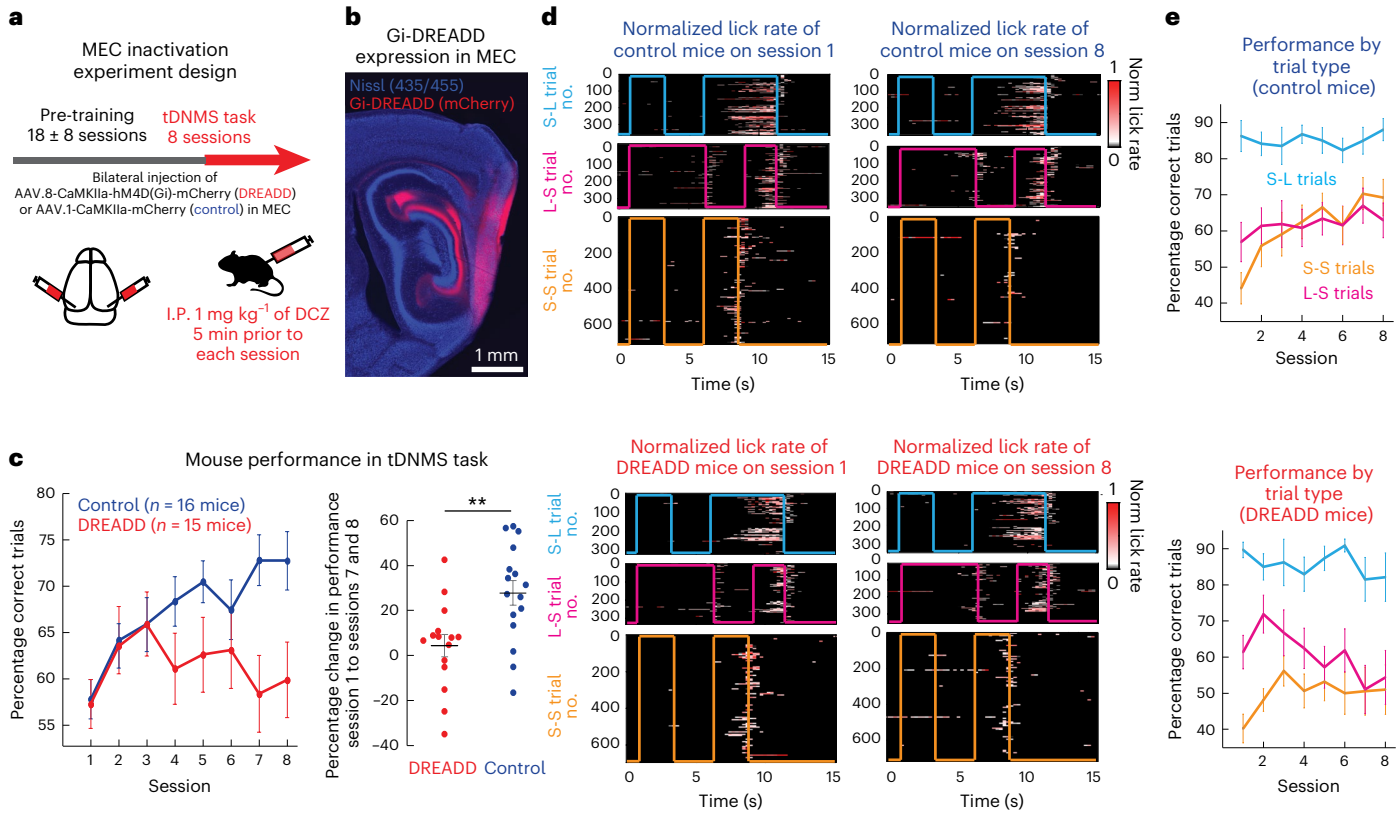

Fig. 4 | MEC is necessary to learn the tDNMS task. a, Experimental paradigm. Mice received bilateral injections of either an inhibitory DREADD ($n = 15$) or control virus ($n = 16$). Mice began pretraining with only nonmatch trials and learned to lick at the offset of the second odor stimuli. After pretraining, mice began the tDNMS task. DREADD agonist DCZ (1 mg kg^{-1}) was administered i.p. 5 min before each of the eight tDNMS sessions. Pretraining sessions are reported as mean ± s.d. **b**, Sagittal section depicting hM4D(Gi)-mCherry expression in MEC with blue Nissl staining; representative image from one mouse. **c**, Left, performance on the tDNMS task for control ($n = 16$) and DREADD ($n = 15$) mice. Values are averaged across mice (mean ± s.e.m.). Right, percentage change in correct responses from day 1 to average of days 7 and 8 ($P = 0.0038$, unpaired, two-tailed Student's t-test). The bars represent mean ± s.e.m. **d**, Top, licking behavior during tDNMS task for all control mice on session 1 (left) and session 8 (right) for all three trial types. Bottom, licking behavior during tDNMS task for all DREADD mice on session 1 (left) and session 8 (right) for all three trial types. Consummatory licking after reward delivery is not shown. **e**, Performance for control mice (top, $n = 16$) and DREADD mice (bottom, $n = 15$) on each of the three trial types, averaged across mice (mean ± s.e.m.).

learning. Indeed, control mice demonstrated a significant increase in S-S trial accuracy across eight sessions (from 44.2 ± 4.3% correct on session 1 to 69.3 ± 5% correct on session 8; repeated-measures ANOVA $F_{7,15} = 5.93$, $P < 0.001$, as shown in Fig. 4e). Interestingly, DREADD mice showed an initial improvement in S-S trials over sessions 1–3 (40.4 ± 4% correct match trials on session 1 versus 56.3 ± 4.2% correct match trials on session 3; repeated-measures ANOVA $F_{2,14} = 8.01$, $P < 0.01$), reflected in their overall learning curve. However, match trial performance did not significantly improve across the eight sessions (repeated-measures ANOVA $F_{7,14} = 0.78$, $P = 0.61$), leveling near 50% (50.7 ± 3.6% correct match trials over sessions 6–8), indicating that mice guessed whether or not to lick. Although control mice learned to use stimulus durations to determine when to withhold licking, DREADD mice perseverated with the rigid strategy of licking at trial offset (Kolmogorov–Smirnov (KS) test on control and DREADD S-S learning curves, $P < 0.01$) (Fig. 4d).

Notably, DREADD mice were not impaired in all aspects of timing behavior. Both control and DREADD mice performed above chance in nonmatch trials, suggesting that MEC is not required to recall well-learned temporal contexts such as 'S-L reward' (Fig. 4e). Mice even engaged in predictive licking in anticipation of a reward (Fig. 4d), further indicating that MEC is not required to perceive or estimate learned durations. The key behavioral difference between control and DREADD mice was that DREADD mice were unable to form a memory of a new temporal structure ('S-S no reward'), leading to an inability to adopt a flexible context-based strategy.

An alternative explanation for our results is that MEC inhibition may not affect the learning of temporal context, but, rather, other aspects of behavior necessary for tDNMS performance. We first considered whether MEC inactivation impaired odor perception. However, the robust performance of DREADD mice on nonmatch trials indicates intact odor perception (Fig. 4d,e). We then examined whether MEC inhibition increased impulsivity, because task learning requires mice to inhibit licking. We compared the average time from trial onset to first lick for both control and DREADD mice across session 1. If MEC inhibition increased impulsivity, DREADD mice should lick earlier. This was not the case (Extended Data Fig. 6c), confirming that MEC inhibition causes a specific deficit in learning context-based timing behavior.

MEC is not necessary for ongoing tDNMS performance

The emergence of context-dependent time cells led us to test, and confirm, the hypothesis that MEC is necessary to learn the tDNMS task. We next wondered whether the role of MEC is confined to learning or whether MEC is also required for ongoing task performance. To distinguish these possibilities, we silenced MEC after task learning. We did this as a continuation of our first MEC inactivation experiment: after eight consecutive sessions of MEC inactivation (Fig. 4), we took mice off DCZ and instead administered saline over sessions 9–14 (Extended Data Fig. 7a), hypothesizing that, without MEC inhibition, mice would learn the task. Indeed, DREADD mice learned the task (repeated-measures ANOVA $F_{5,8} = 3.72$, $P < 0.01$), reaching 77.7 ± 3.9% correct responses over sessions 13 and 14 (Extended Data Fig. 7b). We then administered

https://doi.org/10.1038/s41593-024-01683-7

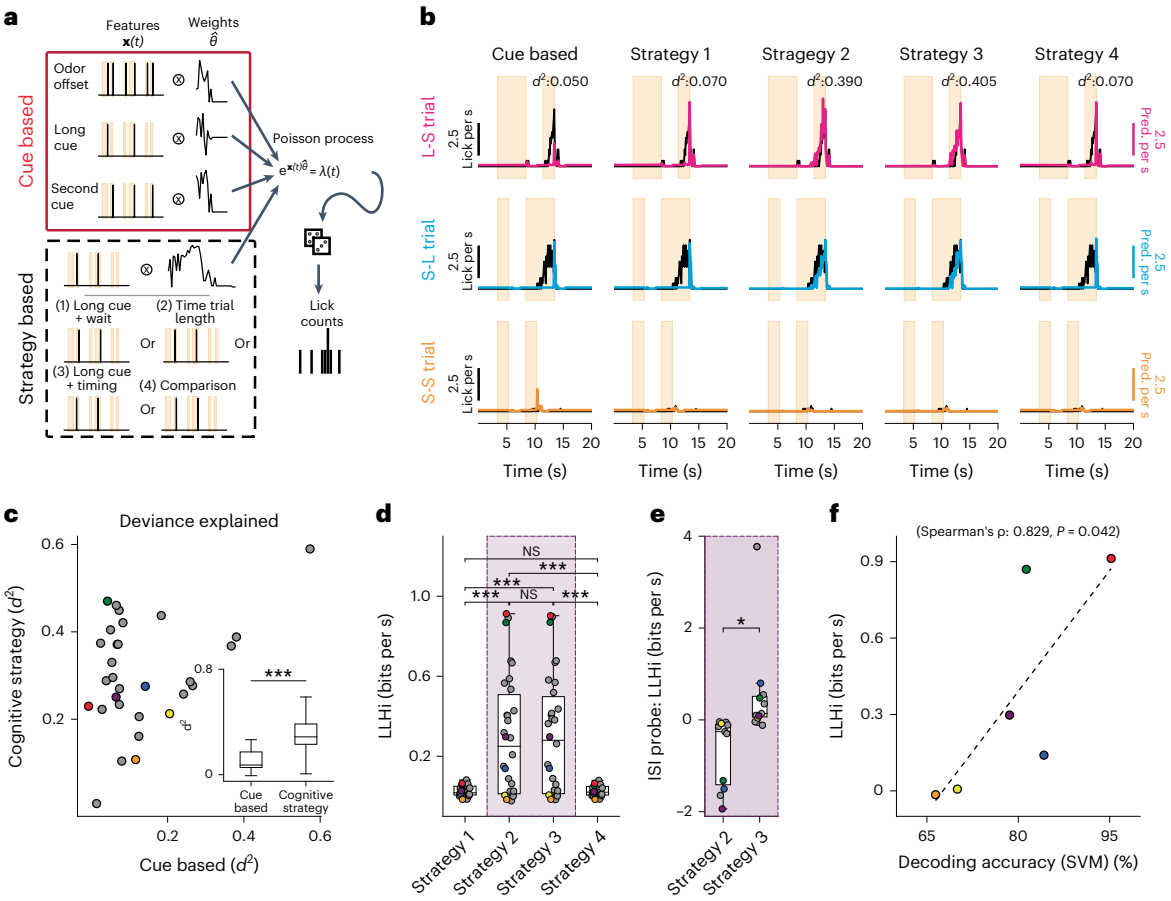

Fig. 5 | Model of behavior demonstrates potential cognitive strategy at use in tDNMS task. a, Model of the animals' behavior as a nonhomogeneous Poisson process. Expected lick counts are based on both event-based cues (odor offset, long odor offset and second cue offset) and a cognitive strategy, which could improve task performance but requires timing longer or multiple durations. For $\mathbf{x}(t)$, lags are not shown. **b**, Comparison of cue-based and several potential strategy-based models for one mouse. Mean lick rate for each trial type is shown in black and model predictions are overlaid in color. **c**, Adding strategy-based features improves model fit to behavior, on average, over only cue-based features. Points from the highest performing strategy-based model are shown. Inset, mean deviance explained (d^2) is higher for strategy-based models ($n = 30$ mice, $p = 3.54 \times 10^{-7}$, two-sided, paired Student's t-test). **d**, Comparison of the LLHi over a cue-based model for the four different potential strategies ($n = 30$ mice, one-way ANOVA: $F = 16.57$, $P = 4.99 \times 10^{-9}$; Tukey's post-hoc test for multiple comparison of means: $^{*}P < 0.05$, $^{**}P < 0.01$, $^{***}P < 0.001$, NS, not significant). **e**, Testing the model on probe trials with manipulated ISI times shows that strategy 3 is more likely than strategy 2 ($n = 11$ mice, $P = 0.03$, two-sided, paired Student's t-test). **f**, Tendency to use more abstract methods during the tDNMS task correlated with neural dynamics in MEC, based on a best-fit strategy and trial-type decoding results ($\rho = 0.83$, $P = 0.04$, two-sided Spearman's rank test for correlation and t-statistic). Colors in **c**–**f** indicate imaged mice and gray indicates not imaged. Center line on box plots depicts the median, the first and third quartiles are indicated by the extent of the box and whiskers indicate the outlier cutoff (1.5× the interquartile range).

DCZ to inhibit MEC over sessions 15 and 16 (Extended Data Fig. 7a,b). Mice did well on sessions 15 and 16 despite MEC inhibition; there was no difference in performance from sessions 13 and 14 to sessions 15 and 16 (2.19 ± 7.3% change in correct response from sessions 13 and 14 to sessions 15 and 16 for DREADD mice; $n = 7$), showing that MEC is not required to perform the tDNMS task after learning (Extended Data Fig. 7b). These results suggest that MEC is specifically necessary to form representations of temporal context; other brain regions can guide post-learning performance.

MEC is not required to learn rigid timing behavior

A key requirement in developing our timing task was cognitive flexibility, given the findings that MTL structures are involved in flexible, not rigid, navigation behavior[4,6,31]. The critical role of MEC in learning the tDNMS task therefore led us to question whether MEC is necessary to learn any temporal relationship or whether MEC is specifically required for flexible tasks requiring distinguishing between temporal contexts. To disentangle these possibilities, we trained DREADD and control mice on a simple, rigid, fixed interval (FI) task, in which a drop of water was delivered to the head-fixed mouse every 10 s (ref. 32). Predictive licking, which increases before the reward, signals an understanding of the task's temporal structure (Extended Data Fig. 7c). To test whether MEC is needed to learn this simple timing task, we administered DCZ before each of five training sessions to inactivate MEC. To assess learning, we calculated the percentage of trials in which mice engaged in predictive licking. Over five sessions, the percentage of trials with predictive licking increased for both control mice (16.1 ± 5.3% on day 1 versus 57.8 ± 7.3% on day 5; repeated-measures ANOVA $F_{4,10} = 7.05$, $P < 0.001$) and DREADD mice (14.7 ± 2.4% on day 1 versus 70.9 ± 4.4 on day 5; repeated-measures ANOVA $F_{4,9} = 36.84$; $P < 0.001$), indicating that mice learned to anticipate the forthcoming reward (Extended Data Fig. 7d,e). In addition, as the sessions progressed, the peak of licking activity for both groups shifted closer to the reward time (Extended Data Fig. 7f), suggesting an improved precision in timing (control: −2.05 ± 0.12 s on day 1 to −0.96 ± 0.16 s on day 5; repeated-measures ANOVA $F_{4,10} = 9.20$; $P < 0.001$; DREADD: −1.73 ± 0.14 s on day 1 to −0.97 ± 0.11 s on day 5; repeated-measures ANOVA $F_{4,9} = 7.75$, $P < 0.001$). There was no significant effect of experimental condition

https://doi.org/10.1038/s41593-024-01683-7

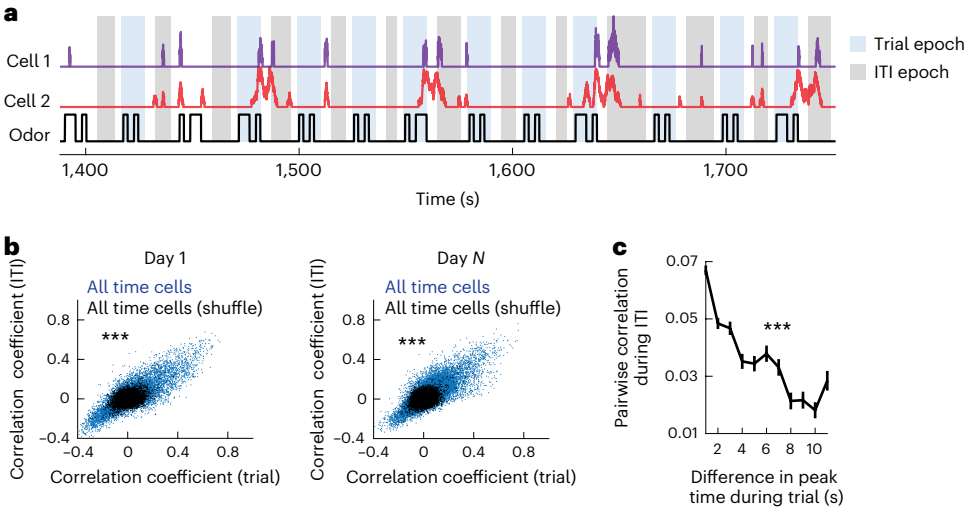

Fig. 6 | Activity correlation between time cells maintained across task and nontask epochs. a, Example time series display for a pair of cells during task and during the ITI. Odor stimuli are shown below. **b**, Left, pairwise correlation between all time cells during the tDNMS task and during the ITI for real (blue) and shuffled data (black) for day 1 recording sessions. Right, same as in left, except shown for day *N* recording sessions (day 1: $n = 11{,}594$, $z = 64.57$, $P = 0$; day *N*: $n = 15{,}727$, $z = 64.57$, $P = 0$, two-sided χ^2 test). **c**, Pairwise correlation of MEC time cells during the ITI as a function of their relative peak timing field activity during the tDNMS task ($n = 27{,}321$, Pearson's correlation coefficient $r = -0.12$, $P = 0$, two sided (mean ± s.e.m.)).

on learning as measured through either the percentage of trials with predictive licking (repeated-measures ANOVA group × time $F = 1.98$, $P = 0.11$; KS test on learning curves, $P = 0.7$) or time of peak licking (repeated-measures ANOVA group × time $F = 1.05$, $P = 0.39$; unpaired Student's *t*-test on day 5 peak lick times, $P = 0.99$), indicating that MEC inhibition did not affect learning. Therefore, MEC is not needed to learn rigid temporal relationships, indicating a specificity in learning context-dependent timing behavior.

The use of cognitive strategies to solve the tDNMS task

The tDNMS task can be solved through multiple strategies, each requiring a varying degree of cognitive flexibility. We sought to (1) identify possible strategies and (2) determine the involvement of MEC in relation to the degree of cognitive flexibility, to provide additional evidence for MEC's role in learning flexible timing behavior. We delineated four cognitive strategies that mice could use to solve the tDNMS task (Methods): (1) identify the long stimulus as a 'go' cue and respond after second odor offset; (2) time the entire trial duration and respond on longer trials; (3) use the long stimulus as a go cue but time both stimuli; and (4) time both stimuli then compare durations. Importantly, these strategies require recognition of the odor, odor, response trial structure. In contrast, mice could employ a simple 'cue-based' approach by learning to lick in response to specific events within a trial without fully grasping its structure, for instance, altering the likelihood of licking after any odor offset. Hallmarks for the use of each approach are present in the licking behavior. Therefore, to evaluate which approach each mouse used, we modeled lick counts as a nonhomogeneous Poisson process based on weighted combinations of cue-based features and each of the strategy-based features (Fig. 5a,b and Extended Data Fig. 9a,b,e). Most mice exhibit behavior that fits better to models with a strategy-based feature (Fig. 5c and Extended Data Fig. 9c), with strategy 2 or 3 yielding the largest increase in model fit (Fig. 5d). To distinguish between these two strategies, we investigated probe trials with manipulated ISIs (Extended Data Figs. 1f and 5). By training our model on the standard ISI trials and testing on the subset with modified ISIs, we found that animals most probably employ strategy 3 (Fig. 5e), which involves using the long stimulus as a go cue but timing both stimuli.

Our modeling also allowed for probing the neural dynamics in MEC time cells to predict the strategy used by each animal. Notably, trial type-decoding performance correlates with the use of a strategy-based approach (Spearman's rank correlation coefficient, $\rho = 0.829$, $P = 0.042$; Fig. 5f). In contrast, no significant relationship exists between decoding accuracy and model fit when also considering the cue-based model ($\rho = 0.600$, $P = 0.208$; Extended Data Fig. 9h). These results indicate that strategies requiring an understanding of trial structure are likely to engage MEC more intensively.

MEC time cells display coherent phasic activity

The present study was inspired from drawing parallels between mechanisms of spatial and temporal coding within MTL structures. There has been a growing body of evidence that a continuous attractor network (CAN), mediated by local recurrent synaptic connectivity in MEC, drives the neural dynamics of spatially selective grid cells[33–36]. We therefore wondered whether MEC time cells might also be driven through the same CAN mechanism. In this model, structured recurrent synaptic connectivity drives an 'activity bump' in a local subpopulation of neurons. This activity bump is then translated across the network as a function of feedforward input, which results in regular phasic activity among neurons in the CAN. A strong prediction of this model is that the relative phasic activity of cells in the network should be coherent during task- and nontask-relevant epochs. To test this prediction of the CAN model, we first measured the pairwise correlations of MEC time cell activity during the tDNMS trial epoch and compared these with the pairwise correlations when mice were not actively timing during the ITI (Fig. 6a). On both day 1 and day *N*, we found that the coherence of pairwise activity between the trial period and ITI is strongly positively correlated and much higher than the chance level (day 1: Pearson's $r = 0.81$ in actual, $r = 0.29$ in shuffle, $P < 0.0001$, $z = 62.65$; day *N*: Pearson's $r = 0.76$ in actual, $r = 0.27$ in shuffle, $P < 0.0001$, $z = 64.57$; Fig. 6b). Next, we sorted MEC time cells according to their relative phases during the tDNMS task and computed the pairwise correlation between MEC time cells during the ITI as a function of the time difference in the peaks of their firing fields in the tDNMS task. Our findings reveal that pairs of MEC time cells active at similar times during the tDNMS task also exhibit a high likelihood of concurrent firing during nontask periods (Pearson's $r = -0.12$, $P < 0.0001$; Fig. 6c). We further repeated the same analysis for correct versus error trials (Extended Data Fig. 10a) and for different trial types (Extended Data Fig. 10b). In all comparisons, we found that time cells exhibited coherent activity across conditions (all *P* values <0.0001). These results are consistent with key predictions of

a local recurrent CAN model that may support the regular, sequential activity of MEC time cells during timing behavior, suggesting that both MEC time and spatial coding neurons could be driven through a common local circuit mechanism.

Discussion

A system capable of episodic memory must track the duration of and between events to form an accurate memory of how experiences unfold over time. However, it remains unclear how MTL structures involved in episodic memory represent temporal relationships of events occurring on the order of interval time (seconds to minutes). Drawing inspiration from spatial literature, we hypothesized that MEC time cells might fire in distinct trajectories to encode the temporal structure of distinct experiences (temporal context). We tested whether previously identified MEC time cells form such trajectories by examining their learning dynamics, testing the predictions that (1) distinct patterns of time cell activity should emerge as animals learn to distinguish temporal contexts and (2) formation of such trajectories should be critical for learning temporal relationships.

Addressing our hypothesis required a multifaceted approach. We first developed a new tDNMS paradigm that requires mice to differentiate the temporal structure of trials. By applying the tDNMS task in tandem with in vivo neurophysiological recordings, we confirmed our ability to record MEC time cells. We confirmed that cells are tuned to elapsed time rather than other features of behavior. We then leveraged the tDNMS task design to ask whether different trial types, or temporal contexts, are represented by differential activity of time cells. Our results showed that time cells were differentially active on distinct trial types, demonstrating that MEC time cells form unique 'timelines' of each context. Crucially, multiple lines of evidence linked the observed timelines to a role in learning of timing behavior. First, we found that populations of time cells exhibit distinct context-dependent neural dynamic trajectories, which diverge from a common trajectory, at key moments in the task when there is sufficient information to disambiguate the trial structure. Second, we found that these trajectories became more distinct over learning across sessions. Third, we showed that, over learning, the population of MEC time cells shifts to over-represent later times in the trial, when the animal can disambiguate trial type and thereby solve the instrumental task. Fourth, on error trials, when the animal mistakenly classifies the trial context, we found that the regular sequence of MEC time cells is disrupted. Finally, we found that MEC inactivation prevents tDNMS learning, specifically by preventing the learning of a new temporal context. Combined, our results indicate that MEC time cells form distinct representations of temporal context, enabling animals to flexibly learn the temporal structure of experiences.

Interestingly, our findings indicate that MEC is not always required for learning and memory of interval timing behavior. MEC is not necessary to learn simple durations, reproduce previously learned durations or recall learned contexts. Rather, MEC is selectively required to learn flexible, context-dependent temporal relationships. This finding fits our physiology data, implying that the role of MEC is to form unique representations of temporal context needed to support such flexible behavior. In further support of this idea, our computational modeling work demonstrates that mice employing a cognitive strategy show increased decoding accuracy of the trial context from the activity of MEC time cells. This specificity of MEC in flexible timing behavior is reminiscent of the finding that MTL structures play a key role in flexible, but not rigid, forms of spatial navigation behavior[21]. Just as multiple memory systems guide navigation[31], we suspect that multiple memory systems guide timing behavior. Previous work has implicated basal ganglia, striatum and frontal and parietal regions in timing[32,37–43], providing evidence of other neural 'clocks' that could drive other aspects of timed behavior. Determination of the constraints under which distinct clocks drive behavior, and interactions between clocks, will be an important step in understanding how the brain performs interval timing.

Previous studies investigating the role of MEC in interval timing have reached slightly differing conclusions about the contribution of MEC. Our observation that MEC is not needed to learn or time fixed intervals appears to contrast with previous work describing roles of MEC in (1) learning to remain immobile for a fixed duration[17], (2) precisely timing a learned duration[19] and (3) delay-dependent timing[18]. To reconcile these differences, we argue that each task involves an element of flexibility, such as (1) updating behavior from a different duration used during pretraining, that is, learning a new temporal context, (2) updating a reference memory after failed trials, that is, updating a memory of temporal context, and (3) making delay-dependent associations, which requires learning temporal context. We expect that the flexibility of learning or updating a memory of temporal context requires MEC, bridging the results of each study. Although our study focused on MEC, other MTL structures, including the hippocampus and lateral entorhinal cortex, also encode time. Previous work has examined temporal coding in various ways, including through explicit timing behavior[44,45], sequence coding[46,47], the delay period of tasks[48,49] and timescales spanning minutes to hours to days[50–52]. Many of these processes occur in parallel, making it difficult to pinpoint precise neural dynamics involved in each aspect of temporal coding. Our study focused on one aspect of temporal coding: interval timing. Given the clear role of MEC in our tDNMS task, a clear future direction will involve testing the necessity of other MTL regions in this task.

Our rationale for examining the role of MEC in interval timing, rather than other MTL structures, stemmed from drawing parallels between spatial and temporal coding. Since the discovery of spatially selective MEC grid cells, there has been a strong focus on the role of MEC in navigation and spatial memory, leading to a research program that has given substantial insight into the circuit mechanisms that underlie grid cell firing. Namely, there is strong support for a CAN that is mediated through structured local recurrent synaptic connectivity of MEC neurons[33–36]. A key feature of this model is that the network integrates synaptic input coding for animal heading direction and velocity, thereby driving sequential activity of a population of grid cells, each coding for different spatial phase(s) within an environment. This process is mathematically equivalent to path integration[33,53], giving rise to a measure of distance traveled from a start location. We find this computation conspicuously similar to that of a clock, which, rather than a measure of distance, can integrate a constant input to give rise to a measure of duration from a start time. A strong prediction of the CAN model is that neurons encoding similar phases while engaged in a relevant behavioral task, such as firing at similar locations in space during navigation or similar delay times during interval timing, will display coherent phasic activity during nontask-relevant epochs. Consistent with this prediction, we found that the correlational structure of MEC time cells, as defined during the tDNMS task, remains coherent during the ITI when there is no timing demand. We suspect that, during timing, the sequential activity of MEC time cells is driven through similar CAN dynamics, which may have evolved for similar and often overlapping navigation processes across time and space. Accordingly, our findings suggest that MEC neurons may serve as a general integration circuit, calculating either distance or time based on relative behavioral demands.

Online content

Any methods, additional references, Nature Portfolio reporting summaries, source data, extended data, supplementary information, acknowledgements, peer review information; details of author contributions and competing interests; and statements of data and code availability are available at https://doi.org/10.1038/s41593-024-01683-7.

References

1. Tulving, E. Précis of elements of episodic memory. *Behav. Brain Sci.* **7**, 223–238 (1984).
2. Tulving, E. *Organization of Memory* (Academic Press, 1972).
3. Kimble, D. P. The effects of bilateral hippocampal lesions in rats. *J. Comp. Physiol. Psychol.* **56**, 273–283 (1963).
4. Niki, H. Response perseveration following the hippocampal ablation in the rat. *Jpn Psychol. Res.* **8**, 1–9 (1966).
5. O'Keefe, J. & Conway, D. H. Hippocampal place units in the freely moving rat: why they fire where they fire. *Exp. Brain Res.* **31**, 573–590 (1978).
6. Olton, D. S., Walker, J. A. & Gage, F. H. Hippocampal connections and spatial discrimination. *Brain Res.* **139**, 295–308 (1978).
7. O'Keefe, J. & Dostrovsky, J. The hippocampus as a spatial map. Preliminary evidence from unit activity in the freely-moving rat. *Brain Res.* **34**, 171–175 (1971).
8. Hafting, T., Fyhn, M., Molden, S., Moser, M.-B. & Moser, E. I. Microstructure of a spatial map in the entorhinal cortex. *Nature* **436**, 801–806 (2005).
9. Muller, R. U. & Kubie, J. L. The effects of changes in the environment on the spatial firing of hippocampal complex-spike cells. *J. Neurosci.* **7**, 1951–1968 (1987).
10. Fyhn, M., Hafting, T., Treves, A., Moser, M.-B. & Moser, E. I. Hippocampal remapping and grid realignment in entorhinal cortex. *Nature* **446**, 190–194 (2007).
11. O'Keefe, J. & Nadel, L. *The Hippocampus as a Cognitive Map* (Oxford University Press, 1978).
12. Buzsáki, G. & Moser, E. I. Memory, navigation and theta rhythm in the hippocampal-entorhinal system. *Nat. Neurosci.* **16**, 130–138 (2013).
13. Kacelnik, A., Brunner, D. & Gibbon, J. *Behavioural Mechanisms of Food Selection* (ed. Hughes, R. N.) 61–82 (Springer, 1990).
14. Marshall, A. T. & Kirkpatrick, K. Reinforcement learning models of risky choice and the promotion of risk-taking by losses disguised as wins in rats. *J. Exp. Psychol. Anim. Learn. Cogn.* **43**, 262–279 (2017).
15. Brunner, D., Fairhurst, S., Stolovitzky, G. & Gibbon, J. Mnemonics for variability: remembering food delay. *J. Exp. Psychol. Anim. Behav. Process.* **23**, 68–83 (1997).
16. Issa, J. B., Tocker, G., Hasselmo, M. E., Heys, J. G. & Dombeck, D. A. Navigating through time: a spatial navigation perspective on how the brain may encode time. *Annu. Rev. Neurosci.* **43**, 73–93 (2020).
17. Heys, J. G., Wu, Z., Allegra Mascaro, A. L. & Dombeck, D. A. Inactivation of the medial entorhinal cortex selectively disrupts learning of interval timing. *Cell Rep.* **32**, 108163 (2020).
18. Vo, A. et al. Medial entorhinal cortex lesions produce delay-dependent disruptions in memory for elapsed time. *Neurobiol. Learn. Mem.* **185**, 107507 (2021).
19. Dias, M., Ferreira, R. & Remondes, M. Medial entorhinal cortex excitatory neurons are necessary for accurate timing. *J. Neurosci.* **41**, 9932–9943 (2021).
20. Heys, J. G. & Dombeck, D. A. Evidence for a subcircuit in medial entorhinal cortex representing elapsed time during immobility. *Nat. Neurosci.* **21**, 1574–1582 (2018).
21. Morris, R. G., Garrud, P., Rawlins, J. N. & O'Keefe, J. Place navigation impaired in rats with hippocampal lesions. *Nature* **297**, 681–683 (1982).
22. Mishkin, M. Memory in monkeys severely impaired by combined but not by separate removal of amygdala and hippocampus. *Nature* **273**, 297–298 (1978).
23. Squire, L. R. & Zola-Morgan, S. The medial temporal lobe memory system. *Science* **253**, 1380–1386 (1991).
24. Otto, T. & Eichenbaum, H. Neuronal activity in the hippocampus during delayed non-match to sample performance in rats: evidence for hippocampal processing in recognition memory. *Hippocampus* **2**, 323–334 (1992).
25. Verhagen, J. V., Wesson, D. W., Netoff, T. I., White, J. A. & Wachowiak, M. Sniffing controls an adaptive filter of sensory input to the olfactory bulb. *Nat. Neurosci.* **10**, 631–639 (2007).
26. Heys, J. G., Rangarajan, K. V. & Dombeck, D. A. The functional micro-organization of grid cells revealed by cellular-resolution imaging. *Neuron* **84**, 1079–1090 (2014).
27. Kraus, B. J. et al. During running in place, grid cells integrate elapsed time and distance run. *Neuron* **88**, 578–589 (2015).
28. Campbell, M. G., Attinger, A., Ocko, S. A., Ganguli, S. & Giocomo, L. M. Distance-tuned neurons drive specialized path integration calculations in medial entorhinal cortex. *Cell Rep.* **36**, 109669 (2021).
29. Turi, G. F. et al. Vasoactive intestinal polypeptide-expressing interneurons in the hippocampus support goal-oriented spatial learning. *Neuron* **101**, 1150–1165.e8 (2019).
30. Hardcastle, K., Maheswaranathan, N., Ganguli, S. & Giocomo, L. M. A multiplexed, heterogeneous, and adaptive code for navigation in medial entorhinal cortex. *Neuron* **94**, 375–387.e7 (2017).
31. McDonald, R. J. & White, N. M. A triple dissociation of memory systems: hippocampus, amygdala, and dorsal striatum. *Behav. Neurosci.* **107**, 3–22 (1993).
32. Toda, K. et al. Nigrotectal stimulation stops interval timing in mice. *Curr. Biol.* **27**, 3763–3770.e3 (2017).
33. Burak, Y. & Fiete, I. R. Accurate path integration in continuous attractor network models of grid cells. *PLoS Comput. Biol.* **5**, e1000291 (2009).
34. Yoon, K. et al. Specific evidence of low-dimensional continuous attractor dynamics in grid cells. *Nat. Neurosci.* **16**, 1077–1084 (2013).
35. Stensola, H. et al. The entorhinal grid map is discretized. *Nature* **492**, 72–78 (2012).
36. Gardner, R. J. et al. Toroidal topology of population activity in grid cells. *Nature* **602**, 123–128 (2022).
37. Matell, M. S., Meck, W. H. & Nicolelis, M. A. L. Interval timing and the encoding of signal duration by ensembles of cortical and striatal neurons. *Behav. Neurosci.* **117**, 760–773 (2003).
38. Hinton, S. C. & Meck, W. H. Frontal-striatal circuitry activated by human peak-interval timing in the supra-seconds range. *Brain Res. Cogn. Brain Res.* **21**, 171–182 (2004).
39. Meck, W. H. Neuroanatomical localization of an internal clock: a functional link between mesolimbic, nigrostriatal, and mesocortical dopaminergic systems. *Brain Res.* **1109**, 93–107 (2006).
40. Jin, D. Z., Fujii, N. & Graybiel, A. M. Neural representation of time in cortico-basal ganglia circuits. *Proc. Natl Acad. Sci. USA* **106**, 19156–19161 (2009).
41. Jazayeri, M. & Shadlen, M. N. A neural mechanism for sensing and reproducing a time interval. *Curr. Biol.* **25**, 2599–2609 (2015).
42. Mello, G. B. M., Soares, S. & Paton, J. J. A scalable population code for time in the striatum. *Curr. Biol.* **25**, 1113–1122 (2015).
43. Bakhurin, K. I. et al. Differential encoding of time by prefrontal and striatal network dynamics. *J. Neurosci.* **37**, 854–870 (2017).
44. Meck, W. H., Church, R. M. & Olton, D. S. Hippocampus, time, and memory. *Behav. Neurosci.* **98**, 3–22 (1984).
45. Jacobs, N. S., Allen, T. A., Nguyen, N. & Fortin, N. J. Critical role of the hippocampus in memory for elapsed time. *J. Neurosci.* **33**, 13888–13893 (2013).
46. Fortin, N. J., Agster, K. L. & Eichenbaum, H. B. Critical role of the hippocampus in memory for sequences of events. *Nat. Neurosci.* **5**, 458–462 (2002).
47. Allen, T. A., Salz, D. M., McKenzie, S. & Fortin, N. J. Nonspatial sequence coding in CA1 neurons. *J. Neurosci.* **36**, 1547–1563 (2016).

48. MacDonald, C. J., Lepage, K. Q., Eden, U. T. & Eichenbaum, H. Hippocampal 'time cells' bridge the gap in memory for discontiguous events. *Neuron* **71**, 737–749 (2011).
49. Pastalkova, E., Itskov, V., Amarasingham, A. & Buzsáki, G. Internally generated cell assembly sequences in the rat hippocampus. *Science* **321**, 1322–1327 (2008).
50. Manns, J. R., Howard, M. W. & Eichenbaum, H. Gradual changes in hippocampal activity support remembering the order of events. *Neuron* **56**, 530–540 (2007).
51. Mankin, E. A. et al. Neuronal code for extended time in the hippocampus. *Proc. Natl Acad. Sci. USA* **109**, 19462–19467 (2012).
52. Tsao, A. et al. Integrating time from experience in the lateral entorhinal cortex. *Nature* **561**, 57–62 (2018).
53. Issa, J. B. & Zhang, K. Universal conditions for exact path integration in neural systems. *Proc. Natl Acad. Sci. USA* **109**, 6716–6720 (2012).

https://doi.org/10.1038/s41593-024-01683-7

Methods

Surgery and behavior

All experiments were approved and conducted in accordance with the University of Utah Animal Care and Use Committee. Animals were housed on a reversed 12 h:12 h light cycle, with a room temperature of approximately 21.1 °C and humidity between 25% and 45%.

MEC microprism implant. Methods for MEC microprism implant have been described previously[20,26]. Camk2a-tTA;tetO-GCaMP6s double transgenic heterozygotes—created by crossing B6;DBA-Tg(tetO-GCaMP6s)2Niell/J and B6.Cg-Tg(Camk2a-tTA)1Mmay/DboJ (Jackson Laboratory)—were used for calcium-imaging experiments. DREADD validation experiments were performed in two mice (one male, one female, aged 4–5 months). To examine neural activity in the tDNMS task, six mice (five males and one female, one aged 17 weeks and five 6–8 weeks on the date of surgery) were used. Briefly, mice were anesthetized using 1–2% isoflurane. An approximately rectangular craniotomy was made over the dorsal surface of the cortex (above the MEC) and cerebellum with corners positioned as follows: (1) ~2.1 mm lateral to bregma, ~4.5 mm caudal to bregma (~300–500 µm rostral to the transverse sinus); (2) ~4.5 mm lateral to bregma, ~4.5 mm caudal to bregma (~300–500 µm rostral to the transverse sinus); (3) ~2.1 mm lateral to bregma, ~7.75–8 mm caudal to bregma (~3.25–3.5 mm caudal to the transverse sinus); and (4) ~4.5 mm lateral to bregma, ~7.75–8 mm caudal to bregma (~3.25–3.5 mm caudal to the transverse sinus). After the skull was removed, a portion of the cerebellum was aspirated to expose the caudal surface of the cortex. The tentorium separating the cerebellum and cortex was carefully removed, leaving the dura of the cortex completely intact. A microprism (right-angle prism with 1.5-mm side length and reflective enhanced aluminum coating on the hypotenuse; Tower Optical) was mounted on a customized stainless-steel mount (using ultraviolet light-curable adhesive; Norland). This assembly was then positioned by aligning the front face of the microprism parallel with the caudal surface of the MEC and the top surface of the microprism perpendicular to the (eventual) axis of excitation light propagation. A thin layer of Kwik-Sil was applied to the caudal MEC surface before microprism implantation to fill the void between the brain and the front surface of the microprism. The microprism and mount were rigidly held in place and the craniotomy sealed by application of a thin layer of Metabond to all exposed sides of the microprism (except the top surface of the prism) and mount and on any exposed skull or brain. A titanium headplate (9.5 × 38 mm^2) was then attached to the dorsal surface of the skull, centered on and aligned parallel to the top face of the microprism. A titanium ring (27-mm outer diameter and 12.5-mm inner diameter, with a 3-mm high edge) was then attached to the top surface of the headplate, centered around the microprism, and the area between the craniotomy and the inner edge of the metal ring was covered with opaque dental cement (Metabond, Parkell; made opaque by adding 0.5 g of carbon powder, Sigma-Aldrich).

AAV injections. To inhibit MEC, C57BL/6 mice obtained from Charles River (n = 40 mice: 20 males and 20 females; postnatal 2–3 months) were injected bilaterally with pAAV-CaMKIIa-hM4D(Gi)-mCherry (Addgene: AAV8; 2.40 × 10^{13} genome copies (GC) ml^{-1}; diluted 1:1 in phosphate-buffered saline (PBS)) or pAAV-CaMKIIa-mCherry (Addgene: AAV1; 1.40E × 10^{13} GC ml^{-1}; diluted 1:1 in PBS). A Nanoject III Injector (Drummond) was used to inject 80 nl of virus (divided into 4× 20-nl injections, injected at a rate of 10 nl s^{-1}) at 6 sites in each hemisphere. Injections were targeted at: 2.9 mm lateral from bregma and 0.15 mm rostral to the transverse sinus; 3.3 mm lateral from bregma and 0.15 mm rostral to the transverse sinus; and 3 depths (1.2 mm, 1.6 mm and 2 mm) from the dorsal surface of the brain.

Experimental setup for tDNMS task establishment and DREADD inactivation experiments. Mice were head-fixed over a cylindrical treadmill (60-cm circumference and 10-cm width), which was enclosed in a box (60 cm length × 60 cm width × 63.5 cm height). After being head-fixed, an odor nozzle and lick spout were placed near the mouse. Odorized air was delivered using a flow dilution olfactometer[25]. The olfactometer consisted of two streams of air: a carrier stream (0.9 l min^{-1}) and an odorized stream (50 ml min^{-1}) which carried isoamyl acetate (2% isoamyl acetate in mineral oil; odorant from Cole-Parmer, 99+%). The two streams combined and a solenoid valve was used to direct the odorized airflow either to the mouse (via the odor nozzle) or to a vacuum (1.8 l min^{-1}). Odor delivery was validated using a photoionization detector. Licking was monitored throughout each training session and was detected using a capacitance sensor (SparkFun Capacitive Touch, catalog no. AT42QT1010) with an electrode positioned on the lick spout. A solenoid valve was used to deliver water (~6 µl per drop) via the lick spout when appropriate. All experimental paradigms were automated and controlled using an Arduino Uno and data collection was performed using a Picoscope Oscilloscope (Pico Technology, v.6.13.2, catalog no. PICO4824) sampling at 1 kHz. Mice were free to run on the treadmill during all training sessions. Behavioral training was performed in the dark, during the dark phase of the animals' light cycle.

Behavioral training. After recovering from surgery, mice began water restriction (~1 ml of water per day). Once mice reached ~85% of their initial weight, they began pretraining for the tDNMS task. Mice were first acclimated to the experimental setup though a habituation phase. During habituation, series of 50 drops of water (3 s apart) were delivered to the mouse (3–6 series of 50 drops per session). Habituation ended after the mice licked to consume ≥80% of water drops in a series of 50 drops. After habituation, mice began three phases of shaping: shaping 1, shaping 2 and shaping 3. Shaping followed the same trial structure of the tDNMS task; however, only nonmatch trials were used. Each trial consisted of a flash of green light (lasting 0.25 s in duration and preceding odor onset by 3 s) to alert mice that the trial was about to start, the first odor, an ISI, the second odor and a response window. Trials were separated by a random ITI (ranging from 16 s to 24 s). In shaping 1, a drop of water was automatically delivered 0.25 s after the second odor offset in each trial. Once the mice licked to consume drops in ≥80% of trials, they progressed to shaping 2. Probe trials were introduced in shaping 2. During probe trials, the mouse had to lick within a 3-s response window after the second odor offset to trigger a reward. If the mouse successfully triggered a reward, the next trial was another probe trial. If the mouse failed to trigger a reward in a probe trial, the next trial was automatically rewarded, after which the mouse was given another probe trial. Training on this phase continued until mice licked to earn a reward in ≥20 consecutive trials. Mice then began shaping 3, which had the same probe trial format as shaping 2. However, in addition to licking in the response window, mice were also required to withhold licking during the first odor and ISI to trigger reward delivery. Training on this phase continued until mice reached 2 consecutive sessions of ≥20 consecutive rewarded trials, after which they began the tDNMS task. Some mice failed to reach this benchmark yet routinely performed above chance on probe trials. These mice instead began the tDNMS task after reaching ≥80% correct performance on probe trials. After shaping, mice began the tDNMS task, where match trials were introduced. Match and nonmatch trials were included in a pseudo-random manner and balanced so that half the trials were match and half were nonmatch. Nonmatch trials were evenly split between S-L and L-S trials. Mice were rewarded in nonmatch trials only if they withheld licking during the first odor and ISI and if they licked within the 3-s response window after the second odor offset. Mice received no reward in match trials and were punished with an increased ITI (+12 s) for licking in the response window. Mice were trained for one session per day, with each session consisting of 100 trials for shaping or 90 trials for the tDNMS task. Mice were trained at least 5 d a week during pretraining and 7 d a week during the tDNMS task. The tDNMS learning was assessed by examining performance over the first eight sessions,

by which point performance begins to plateau (Extended Data Fig. 7b; no significant improvement from extended training across sessions 8–14: repeated-measures ANOVA $F_{6,10} = 0.45$, $P = 0.84$).

Several cohorts of mice (C57BL/6 mice obtained from Charles River, balanced male and female, postnatal 2–3 months) were used to establish the tDNMS task (Fig. 1), with minor variations between cohorts. For the first cohort, the light cue indicating trial start was 0.25 s before first odor onset and each upcoming trial was assigned based on probability (25% chance of S-L, 25% chance of L-S, 50% chance of S-S). Subsequent mice were trained on the standard version of the task. In the standard task, the light cue indicating trial start appeared 3 s before the first odor onset. In addition, trials were presented in a block structure: each block of four trials consisted of two S-S trials, one S-L trial and one L-S trial, presented in a random order.

MEC inactivation experiments (Fig. 4) were performed in two cohorts of mice. Each cohort contained a balanced number of control and DREADD mice, with the experimenter blind to experimental conditions. After tDNMS training, the first cohort of mice was trained for an additional session of 30 trials with no odor (mineral oil only) to ensure that mice use odor to solve the task. The second cohort of mice was trained for 16 sessions to test the role of MEC after task learning, and then was subsequently trained on an FI task[32] to determine whether MEC is necessary to learn more rigid timing behavior. Mice that did not meet the criteria to advance beyond shaping, and thus were not trained on the tDNMS task, were also trained on the FI task. The same experimental apparatus was used for the FI task with the exception of odor delivery. In each session of the FI task, a (~6 µl) drop of water was delivered to the head-fixed mouse every 10 s (150 drops per session). Mice were trained for one session per day for 5 d on the FI task.

Imaging data were collected from separate cohorts of mice. Imaging was performed using transgenic mice expressing GCaMP6s under the CaMKIIa promoter. Two mice were used to validate the efficacy of DREADD-mediated inhibition in MEC and were not trained on the tDNMS paradigm. Six mice were implanted and then underwent tDNMS training. To determine how time cells adapted to changes in trial structure, mice were tested on a probe session after tDNMS learning in which the ISI was lengthened from 2 s to 5 s during the last half of the session.

A final, separate cohort of mice (C57BL/6 mice obtained from Charles River, equally balanced male and female, postnatal 2–3 months) was trained on a version of the tDNMS task with modified durations. As a result of the three trial-type design, mice could solve the tDNMS task by learning to lick if the total trial duration was long and to withhold if the total trial duration was short. Standard experiments were performed with a 2-s short odor, 3-s ISI and 5-s long odor, making nonmatch trials 10 s and match 7 s. To test whether mice used a rigid strategy, we decided to introduce probe trials that cause match and nonmatch trials to be the same overall duration. With our standard durations, this would mean lengthening the ISI on match probe trials by 3 s. However, this change would increase task difficulty (increasing the time the mouse must resist impulsivity and increasing working memory demand), making it difficult to determine whether a potential drop in performance is caused by increased task difficulty or use of a rigid strategy. To avoid this problem, we instead trained a separate cohort of mice on a version of the task with 3-s short odors, 5-s ISI and 6-s long odors so that we could reduce the ISI in nonmatch probe trials (randomly chosen half of nonmatch trials) to equal the total trial duration of match trials.

Two-photon imaging of MEC neurons. After mice were pretrained on the tDNMS task (14.5 ± 3.9 d of pretraining), we began two-photon laser resonance scanning of populations of neurons expressing GCaMP6s through the microprism using a Neurolabware microscope. Data were acquired with an 8-kHz resonant scanner, images were collected at a frame rate of 30 Hz with bidirectional scanning and Scanbox software was used for microscope control and data acquisition. A Ti:Sapphire laser (Discovery with TPC, Coherent) at 920 nm was used as the excitation source, with average power measured at the sample (after the objective; ×20/0.45 numerical aperture (NA) air immersion objective (LUCPanFL, Olympus) with correction collar set at 1.25) of 50–120 mW. Imaging was also tracked using a PicoScope Oscilloscope sampled at 1 kHz to synchronize data with behavior.

Histology. After the behavioral experiments, mice were perfused using 4% paraformaldehyde (PFA) in 0.1 M PBS. The brain was removed and fixed in 4% PFA in 0.1 M PBS for ~24 h. Brains were rinsed 3× with 0.1 M PBS, then stored in PBS for 1+ d before the tissue was sectioned into 50- to 100-µm sagittal slices using a vibrating microtome. Free floating slices were then incubated in 0.1 M PBS with 0.1% Triton-X for 15 min, washed with 0.1 M PBS and incubated for 3 h in a 25:1 solution of 0.1 M PBS with 435/455 blue or 530/615 red fluorescent NeuroTrace Nissl stain (Invitrogen). Brain sections were imaged and stitched using a VS200 Virtual Slide fluorescence microscope (Olympus) with a ×10 OFN26.5, NA 0.40 objective.

Data analysis

Data acquisition and analysis. Behavioral data were collected using a PicoScope Oscilloscope, then subsequently analyzed in MATLAB (2018b). Imaging data were acquired using Scanbox v.4.1 and analyzed on a IBuyPower Intel Core with Windows10 and customized software written in MATLAB (2018b). Licking behavior was modeled using customized code in Python v.3.11.4.

Behavioral performance. Performance on the tDNMS task was analyzed by determining the percentage of trials in which mice behaved correctly. Correct nonmatch trials were defined as those in which mice withheld licking during the first odor and ISI and licked in the 3-s response window after the second odor offset to trigger reward. Correct match trials were defined as those in which mice withheld licking for the duration of the trial. Mice that met the criteria to advance beyond shaping and begin the tDNMS task were included in the analysis. However, a subset of mice was removed from analysis owing to: a failure to retain the task structure learned in shaping (performance >3 s.d. below the mean on tDNMS session 1, $n = 1$ mouse), headplate falling off ($n = 1$ mouse) or lack of virus expression ($n = 2$ mice). Although most behavior was analyzed as the percentage correct trials, licking behavior was further examined in some instances. Licking was analyzed by identifying lick events, defined as samples (sampling rate of 1 kHz) in which the capacitance sensor detected a signal. For tDNMS behavior, any licking after reward delivery was removed to focus on predictive and not consummatory licking. Lick events were then binned in 0.25-s bins, normalized to the maximum within the session. Lick events were also used to examine performance in the FI task. Performance on the FI task was measured as the percentage of trials in which mice engaged in predictive licking, where predictive licking is defined as an increase in lick events (determined by a significantly positive slope) in the 5 s preceding reward delivery. Precision in the FI task was estimated by determining time of peak licking activity of each mouse on each session. Licking data were binned in 0.25-s bins, and the bin number with the maximum number of lick events was recorded for each of the 150 trials. These values were then averaged and converted to time to give an estimate of peak lick time across the session.

Image processing, ROI selection and transient analysis. In vivo two-photon data sets were acquired during the tDNMS task (120,000 frames per session). Videos were first motion corrected using whole-frame crosscorrelation, as described previously[26] and the motion-corrected time series was used for all subsequent analysis. Regions of interest (ROIs) were defined using Suite2P v.0.10.1 (ref. 54). Significant Ca^{2+} dF/F transients were identified using previously described methods[20,26,55].

Defining time cells in the tDNMS task. Cells exhibiting significant tuning at specific time points during trials were defined based on mutual information[56,57]. Before computing mutual information, Ca^{2+} signals were normalized in each trial by dividing their peak dF/F value to prevent one or two large transients determining a cell's activity pattern. Subsequently, dF/F values were averaged across correct trials and mutual information for the averaged dF/F was calculated using the following equation for each trial type (for example, S-S, S-L, L-S):

$$\text{Mutual information} = \sum_i p_i \lambda_i \log_2 \frac{\lambda_i}{\lambda}$$

where i denotes bin, p_i is the occupancy rate in the ith bin, λ_i is dF/F at the ith bin and λ is the mean dF/F. To determine whether the mutual information significantly exceeded that expected by random activity, the dF/F values for each trial were circularly shifted by a random amount and mutual information was then computed using the shuffled data. Shuffling was repeated 1,000×. The P value was defined as the proportion of shuffled mutual information greater than or equal to real mutual information. Cells were classified as active cells if the mean d$F/F > 0.03$ and the active cells were classified as time cells if the P value of mutual information <0.01.

Comparing correlation between match and nonmatch trial types across day 1 to day *N*. Time cells in either S-S or S-L trial types were selected and Pearson's correlation coefficient between these two trial types was calculated for each cell. The same procedure was performed using time cells in either S-S and L-S trial types. All correlation coefficients were pooled and compared between day 1 and day N using Wilcoxon's rank-sum test.

Population vector differences between match and nonmatch trial types across trial epoch. Time cells in either S-S or S-L trial types were selected. Population vectors were constructed from dF/F of all selected cells at each time bin. The difference in dF/F between S-S and S-L trial types was then computed for each time bin. A corresponding shuffle distribution was generated by randomly assigning trial types and obtaining the dF/F difference 10,000×. The time bin where the actual data exceeded the top 0.1% of the shuffled distribution was considered the significant discrimination timepoint for the trial type. The discriminant index was determined from the summation of the difference between the actual and averaged shuffle values from 8 s to 11 s. This index represents the extent to which the actual dF/F distinguishes between trial types compared with the chance level. The same procedure was repeated for time cells in either S-S or L-S trial types.

Decoding trial type using *k*-means clustering. The k-means clustering was employed to assess the segregation of neural ensemble activity across different trial types. For each trial, population vectors were created by averaging dF/F during the late phase of trials (9–11 s). To prevent overfitting, we reduced the dimensionality of the population vectors to 30 using principal component analysis. The first two linear discriminant components were then determined, forming the axis for the two-dimensional LDA plot (Fig. 3g). Next, the k-means clustering method was applied to this two-dimensional plot to classify trials into three clusters (Extended Data Fig. 4a). Decoding accuracy was assessed by calculating the proportion of correctly classified trials. To establish a baseline, the same procedure was repeated 10,000× with shuffled trial types to generate a corresponding chance distribution. The P value was then computed as the proportion of shuffle values equal to or greater than the actual accuracy of decoding.

Decoding trial type using the SVM. A classifier for each day N session was developed using the SVM and the MATLAB function fitecoc. Only correct trials were used in this analysis. Mean dF/F of time cells during either the early (0–2 s) or the late (9–11 s) phase of trials was used as an input matrix for the fitecoc function. The response input (Y input) for this function was either trial type (that is, S-S, S-L, L-S) or match versus nonmatch of the training trials. The classifier computed from fitecoc then fed to the predict function to obtain decoded responses (for example, S-S type) corresponding to the testing dataset. We applied a leave-one-out crossvalidation method, so the classification process was repeated as the number of entire trials. In each iteration, a single trial was selected for the testing dataset and the rest of the trials were assigned for the training dataset. To calculate the chance level of decoding accuracy shown in Fig. 3h, the response input for the classifier (that is, trial types or match versus nonmatch) corresponding to the training trials was shuffled when creating the classifier. This process was repeated 1,000× to make a distribution of decoding accuracy for shuffled data. The bootstrap P value was determined as the proportion of decoding accuracies in the shuffled distribution that were equal to or greater than the accuracy of the actual dataset.

Measuring activity coherence in error trials. As a result of the low number of error trials in S-L and L-S trials, this analysis was applied only to S-S trial data. Correct trials were divided into two groups using a random subset of trials (correct A and correct B). The number of trials assigned to correct B was set to match the number of error trials. Cell activity was sorted according to the sequence in correct A and correlations for each cell's activity were computed for correct A versus correct B (blue in Fig. 3j) and correct A versus error (red in Fig. 3j). Random sampling of trials was repeated 1,000× to obtain a distribution of correlation coefficients. Then, the mean values of these correlation coefficients were taken as the cell's correlation coefficient values. To compare day 1 with day N, Pearson's correlation coefficient between averaged dF/F on S-S error trials and correct trials of each trial type was calculated for S-S time cells (Extended Data Fig. 4c). To ensure a consistent number of trials for comparison, seven trials were randomly selected and used to compute the averaged dF/F. The resulting sets of correlation coefficients were then compared across sessions (that is, day 1 versus day N) and trial types using a two-way mixed ANOVA.

Comparing variance across time and distance. The dF/F values for time cells were re-charted based on the elapsed running distance from the moment that the trial initiation light was turned on. For each trial, we measured the peak dF/F location within the distance dimension. The variability of these peak locations was assessed using the CV, which is the ratio of the s.d. to the mean and provides a standardized measure of dispersion. This method allows for the comparison of variations across different scales or dimensions. After this, the procedure was applied similarly to measure the elapsed time since the initiation light was activated. The CVs for the time cells were then compared between the distance and time dimensions using a paired Student's t-test.

Generalized linear model. To determine the individual contributions of different behavioral variables (D, T and L) in predicting the activity of MEC neurons, we employed a GLM. This model fits calcium activity (dF/F) as a Gaussian linear function using various combinations of these three behavioral variables[29,30]. For the dF/F data of each cell in each trial type (S-S, S-L and L-S), we developed seven models. These included three single-variable models (D, T, L), three double variable models (TD, TL, DL) and one comprehensive model (TDL). We utilized data from ten recording sessions to perform this modeling.

In our model, distance is represented by ten binary variables, corresponding to ten spatial bins, with each bin equal to one when the animal occupied that spatial bin and zero otherwise. Time and licking are represented in the same way by ten and two binary variables, respectively. The dF/F was then smoothed with a Gaussian kernel. Models were fit using the MATLAB fitglm function with a fivefold crossvalidation procedure. We then calculated the LLH increase (LLHi) for each

model as follows: where N is the number of data points, $\widehat{dF/F}$ is the model predicted dF/F and $\overline{dF/F}$ the session mean dF/F. LLH is normalized by recording time (per min).

$$\mathrm{LLH}_{\mathrm{model}} = -\frac{N}{2}\ln 2\pi\sigma^2 - \frac{1}{2\sigma^2}\sum_i^N \left(dF/F_i - \widehat{dF/F_i}\right)^2$$

$$\mathrm{LLH}_{\mathrm{mean}} = -\frac{N}{2}\ln 2\pi\sigma^2 - \frac{1}{2\sigma^2}\sum_i^N \left(dF/F_i - \overline{dF/F}\right)^2$$

$$\mathrm{LLH} = \mathrm{LLH} \times \text{Sampling rate} \times 60/N$$

$$\mathrm{LLHi} = \mathrm{LLH}_{\mathrm{model}} - \mathrm{LLH}_{\mathrm{mean}}.$$

To select the model that best described the calcium activity of each cell, we first found the single-variable model with best performance, then determined whether any double variable models that included this single variable had better performance. If so, we then compared the double variable model with the full model. Model performance was determined by comparing the LLHi using a one-sided signed-rank test, with a significance value of $P = 0.05$. To ensure the significance of the models, we used data from a cell only if its best model has LLHi > 0.

To estimate the specific contribution of each behavioral variable, we found all cells with significant full and double variable models. We then calculated the log-likelihood difference as follows (using time as an example):

If the best model of a cell is the full model:

$$\mathrm{LLH}_T = \mathrm{LLH}_{TDL} - \mathrm{LLH}_{DL}.$$

If the best model is one of the double variable models:

$$\mathrm{LLH}_T = [(\mathrm{LLH}_{TD} - \mathrm{LLH}_D) + (\mathrm{LLH}_{TL} - \mathrm{LLH}_L)]/2.$$

Across all cells and trial types, we identified $N = 177$ significant models (Kruskal–Wallis test followed by Wilcoxon's rank-sum test with Bonferroni's correction, $P < 0.001$ for all). We selected the model that best described the dF/F for each cell and trial type as the model with the highest LLHi, which most often corresponded to a single-variable model of time (125 out of 177 significant models).

Poisson modeling of animals' licking behavior. A Poisson GLM was fit to the anticipatory licking data individually for each mouse to assess animals' internal model for solving the task. Behavioral data were down-sampled to 10 Hz and cropped to 20 s per trial. The expected value for anticipatory lick counts, $\lambda(t)$, was predicted according to a Poisson distribution:

$$\lambda(t) = e^{\mathbf{x}(t)^T\theta}$$

where $\mathbf{x}(t)$ corresponds to the column vector of predictor features in the model at time t and $\boldsymbol{\theta}$ is the vector of weights assigned to each feature's influence on the predicted lick count. Only anticipatory licks were used and any licks after water delivery were omitted.

A no-strategy model was first developed in which mice could learn to modify licking probability based on individual event-based cues. Under this 'cue-based' model, mice could modify licking probability in response to key events: any odor offset, prolonged odor exposure or second odor offset. This cue-based approach could result in licking at key times throughout the trials but could never solve the task with 100% success. The four cognitive strategies were then tested by adding features that corresponded to whether the conditions given by an individual strategy were met. Strategy 1 involves identifying the long stimulus as a 'go' cue and licking after second odor offset. This strategy did not permit predictive licking before the second odor offset. Strategy 2 required timing the entire trial duration, not individual odors, and using total trial duration to solve the task. This strategy could be further assessed using probe trials with manipulated total trial durations. Strategy 3 was similar to strategy 1, in which mice used the long stimulus as a go cue. However, in strategy 3, mice timed both stimuli, allowing predictive licking. Finally, strategy 4 required timing both stimuli and comparing the durations after.

Each strategy was tested individually by adding its features to the cue-based model and calculating the degree of improvement in the model fit to observed licking. For all models, cue-based features were lagged every time bin from 0 s to 2 s and strategy-based features were given lags from 0 s to 12 s to account for any licking between the offset of the second odor until the end of the trial. Estimated weights ($\hat{\boldsymbol{\theta}}$) for each feature were learned using Python's scikit-learn package. We applied L2 regularization to avoid overfitting owing to predictor collinearity and we evaluated the models by k-fold crossvalidation across trials ($k = 10$). Models were scored using the deviance explained (d^2) metric to assess goodness of fit. For models including strategy-based features, we calculated the LLHi over the cue-based model.

Comparing pairwise activity correlation between trial period and ITI. To measure the coherence of MEC time cells across tDNMS trial and nontrial epochs, we compared the pairwise activity of all time cell pairs between the trial period and the ITI[58]. The entire time series of dF/F in a session (for example 120,000 frames) was segmented into 500-ms time bins and dF/F values were summed within each time bin. Time bins from 1 s before the first odor onset to the second odor offset (11 s) were included in the trial period and time bins from 5 s after the second odor offset to 4 s before the next first odor onset were included in the ITI. Given the 3- to 5-s gaps between each trial period and ITI, the likelihood of activity from one epoch influencing the other was minimal. The time bins within these gaps were excluded from the analysis. Kendall's correlation (τ values) was calculated for the series of summed dF/F values during either the trial period or ITI across all pairs of simultaneously recorded time cells. Then, the coherence across trial and ITI epochs was measured by computing Pearson's correlation coefficient between sets of corresponding τ values of the trial period and ITI (Fig. 6b). To generate shuffled data, the dF/F values were circularly shifted by a random amount before computing τ values. The same procedure was repeated for correct versus error trials (Extended Data Fig. 10a) and between different trial types (Extended Data Fig. 10b). In Fig. 6c, the τ values for the ITI were plotted against the difference in peak times of each cell pair during the trial period.

Statistics and reproducibility

No statistical methods were used to predetermine sample sizes. Sample sizes were based on and comparable to previous work[17,20,32]. Statistical tests were used to test statistical significance when appropriate and include ANOVA, Student's t-test, Wilcoxon's rank-sum test, two-sample KS test, χ^2 test, Wilcoxon's signed-rank tests, Spearman's rank correlation, Pearson's correlation and the Kruskal–Wallis test. All statistical tests were two sided unless stated otherwise. For tests assuming normality, data distributions were assumed to be normal, but this was not formally tested. All data in the text and figures are labeled as mean ± s.e.m., unless stated as mean ± s.d.

For MEC inactivation experiments, animals were randomly assigned to experimental condition. The experimenter was blind to the experimental conditions for all training on the tDNMS task but was unblinded before the FI experiment to permit tDNMS data analysis. Inactivation experiments were performed in two cohorts of mice to verify effect reproducibility, with the second cohort successfully replicating the first. Imaging data were also reproducible, given consistent findings across six mice. Mice were excluded from analysis only if the following occurred: failure to meet criteria to move beyond the

shaping phase of the task, failure to retain the task structure learned in shaping (performance >3 s.d. below the mean on tDNMS session 1), headplate falling off during tDNMS task training or lack of on-target virus expression.

Reporting summary

Further information on research design is available in the Nature Portfolio Reporting Summary linked to this article.

Data availability

Data presented in the present study are available upon reasonable request to the corresponding author and will be made publicly available at https://github.com/heyslab/Bigus_Lee_NatNeuro_2024 1.5 years after publication.

Code availability

Code is available at https://github.com/heyslab/Bigus_Lee_NatNeuro_2024 or upon reasonable request to the corresponding author.

References

54. Pachitariu, M. et al. Suite2p: beyond 10,000 neurons with standard two-photon microscopy. Preprint at *bioRxiv* https://doi.org/10.1101/061507 (2017).
55. Dombeck, D. A., Harvey, C. D., Tian, L., Looger, L. L. & Tank, D. W. Functional imaging of hippocampal place cells at cellular resolution during virtual navigation. *Nat. Neurosci.* **13**, 1433–1440 (2010).
56. Skaggs, W., McNaughton, B. & Gothard, K. *Advances in Neural Information Processing Systems* 5 (Morgan-Kaufmann, 1992).
57. Climer, J. R. & Dombeck, D. A. Information theoretic approaches to deciphering the neural code with functional fluorescence imaging. *eNeuro* **8**, ENEURO.0266-21.2021 (2021).
58. Park, E. H., Keeley, S., Savin, C., Ranck, J. B. & Fenton, A. A. How the internally organized direction sense is used to navigate. *Neuron* **101**, 285–293.e5 (2019).

Acknowledgements

We thank D. Dombeck, M. Long and M. Sheffield for valuable comments on earlier versions of this manuscript. We thank M. Wachowiak for generous support in designing and validating the olfactometers used in the present study. The present study was supported by the US National Institutes of Health (NIH) National Science Foundation (NSF), Whitehall Foundation (J.G.H.), Brain and Behavior Research Foundation (J.G.H.), NIH/National Institute of Mental Health (grant no. 1 DP2 MH129958-01 to J.G.H.), NSF CAREER Award (no. IOS-2145814 to J.G.H.), the Basic Science Research Program through the National Research Foundation of Korea (N.R.F.) funded by the Ministry of Education (grant no. RS-2023-00242639 to H.W.L.) and the University of Utah (J.G.H.). The funders had no role in study design, data collection and analysis, decision to publish or preparation of the manuscript.

Author contributions

E.R.B, H.W.L. and J.G.H. designed experiments and wrote the manuscript. E.R.B, H.W.L. and J.S. collected the data. E.R.B, H.W.L., J.S., J.C.B. and J.G.H. analyzed and interpreted the data. E.R.B. and J.G.H. built equipment used to collect the data.

Competing interests

The authors declare no competing interests.

Additional information

Extended data is available for this paper at https://doi.org/10.1038/s41593-024-01683-7.

Supplementary information The online version contains supplementary material available at https://doi.org/10.1038/s41593-024-01683-7.

Correspondence and requests for materials should be addressed to James G. Heys.

Peer review information *Nature Neuroscience* thanks Mehrdad Jazayeri and the other, anonymous, reviewer(s) for their contribution to the peer review of this work.

https://doi.org/10.1038/s41593-024-01683-7

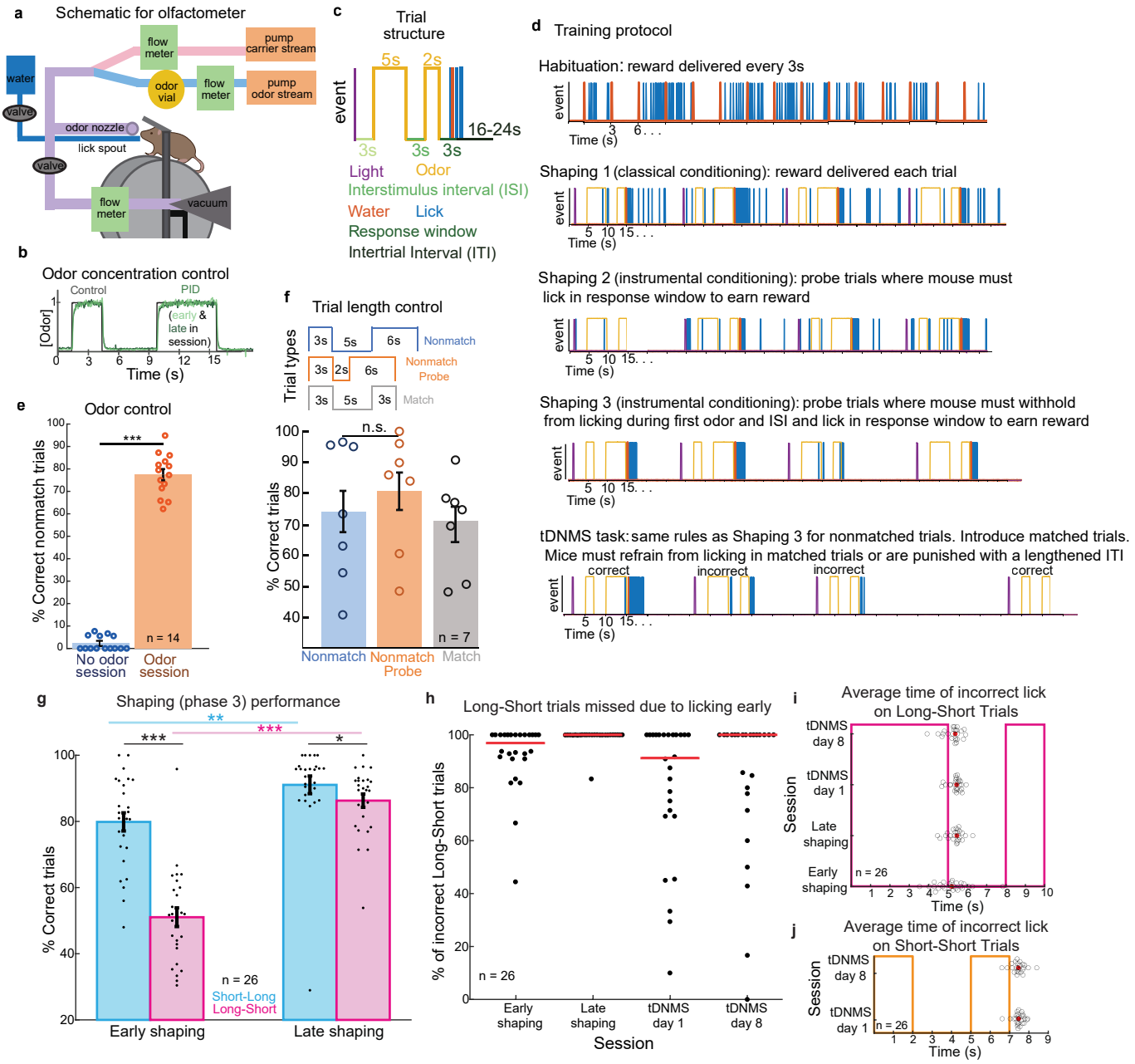

Extended Data Fig. 1 | See next page for caption.

https://doi.org/10.1038/s41593-024-01683-7

Extended Data Fig. 1 | tDNMS set-up, controls, and additional behavioral analysis of mice in Fig. 1. a. Experimental set-up. Odorized air is directed either to the mouse or to a vacuum. A lick spout, connected to a capacitance sensor, delivers water and is used to monitor mouse licking. **b**. Odor concentration control. Odor concentration was measured using a photoionization detector (PID). Odor can be delivered with high temporal specificity at a constant concentration over 45 minutes, as shown by PID measurements (green) relative to control signal (black). **c**. Trial structure. Each trial consists of two presentations of the same odor, each for either a 2 or 5 s duration, separated by an interstimulus interval (ISI). Trial start is signified by a visual cue, and trials are separated by a 16-24 s intertrial interval. **d**. Training protocol. Mice undergo three phases of pretraining (see Methods). **e**. Odor control session. After completing tDNMS training, mice were tested with no odorant (mineral oil only). Mice failed to solve nonmatch trials in the absence of odor but performed well in a prior session in which odor was used ($p = 2.6 \times 10^{-13}$, two-tailed paired t-test; n = 14 mice). Bars represent mean across mice ± s.e.m. **f**. Trial length control session. A cohort of mice was trained on a version of the tDNMS task with modified durations. The ISI was then manipulated on a random subset of nonmatch trials ("probe trials") so that overall trial duration was identical to match trial duration. If mice use total trial duration to solve the task, rather than individual stimulus durations, they should incorrectly withhold licking on probe trials. Instead, there was no significant difference between standard nonmatch and probe trial performance ($p = 0.19$, two-tailed paired t-test; n = 7 mice). Bars indicate mean across mice ± s.e.m. **g**. Average performance by trial type during shaping (phase 3) of mice in Fig. 1 (n = 26). Shaping consists of probe trials where mice must correctly trigger reward and automatic trials where reward is automatically delivered. Performance was examined on all probe trials within the first 1/2 session of shaping phase 3, termed "early shaping", and the last 1/2 session of shaping phase 3, or "late shaping", for each mouse. Dots represent performance of each mouse, and bars show mean ± s.e.m. across mice. Mice performed better on short-long trials than long-short both early ($p = 4.3 \times 10^{-7}$, two-tailed paired t-test) and late ($p = 0.041$, two-tailed paired t-test) in shaping. Additionally, performance was higher for both short-long ($p = 0.009$, two-tailed paired t-test) and long-short ($p = 4.7 \times 10^{-10}$, two-tailed paired t-test) trials in late compared to early shaping. **h**. Reason for mistakes on long-short trials for mice in Fig. 1 (n = 26). During shaping phase 3 and the tDNMS task, mice can miss nonmatch trials either by withholding licking or by licking prematurely during the first odor and/or interstimulus interval. The percent of incorrect long-short trials in shaping phase 3 and the tDNMS task missed due to licking early is shown. Dots indicate values for each mouse, with red lines showing the median value across mice. **i**. Average time of first incorrect lick on long-short trials relative to first odor onset for mice in Fig. 1 (n = 26). Black circles represent the average time of first lick across all incorrect long-short trials for a given mouse, and red dots show the median value across mice. **j**. Average time of first incorrect lick on short-short trials in the tDNMS task relative to first odor onset for mice in Fig. 1 (n = 26). Black circles represent the average time of first lick across all incorrect short-short trials for a given mouse, and red dots show the median value across mice.

https://doi.org/10.1038/s41593-024-01683-7

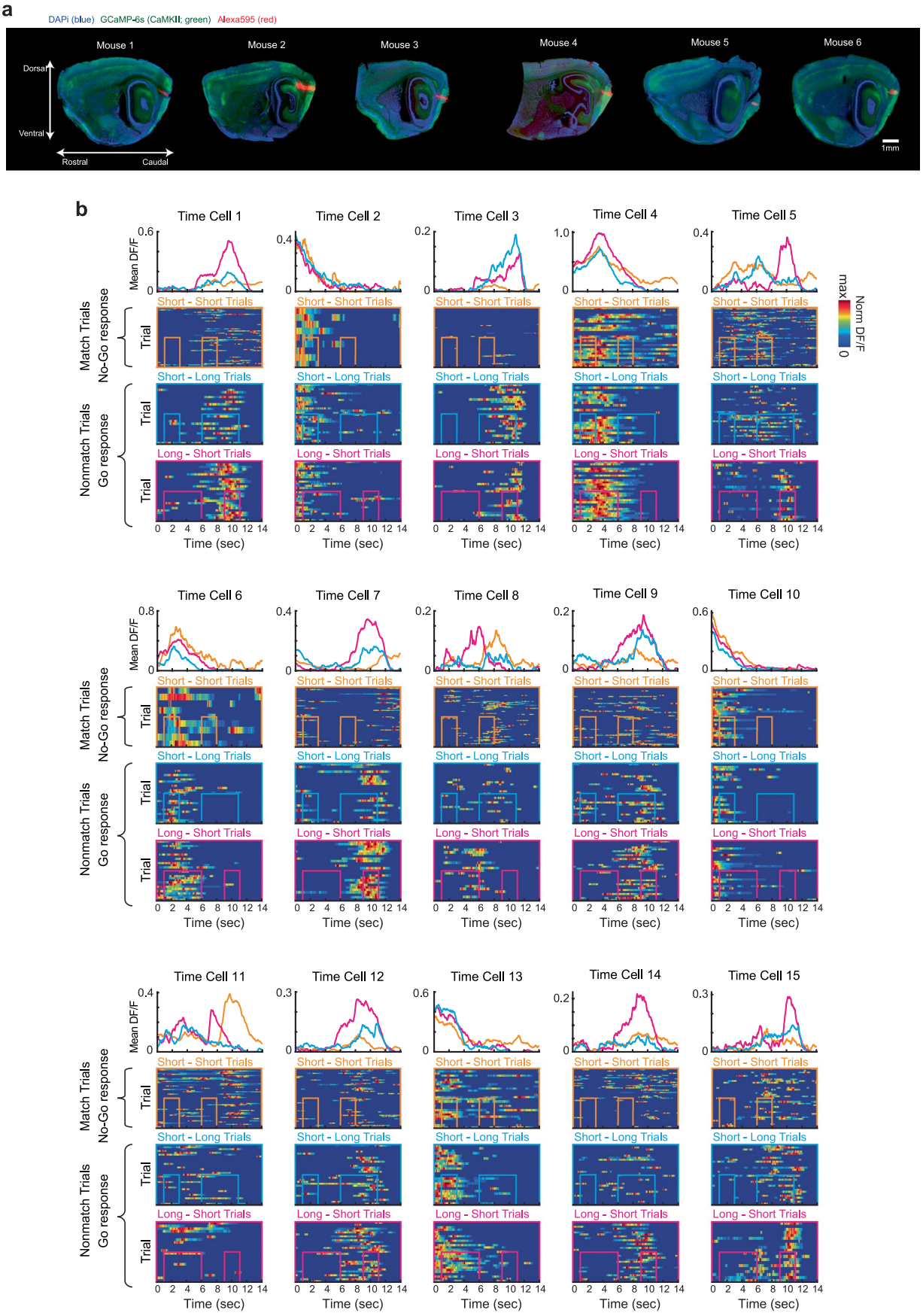

Extended Data Fig. 2 | See next page for caption.

https://doi.org/10.1038/s41593-024-01683-7

Extended Data Fig. 2 | Histological verification of in vivo imaging in the MEC, and additional examples of MEC time cells. a. Sagittal sections of post-mortem histology from all six mice utilized in the in vivo calcium imaging experiments. MEC neurons labelled with GCaMP6s (green). The sections are stained with NeuroTrace 435/455, displaying neuronal morphology in blue. The approximate locations of the two-photon imaging fields of view (FOV) for each mouse are labeled with red Alexa594. This labeling was achieved by inserting a pin coated with Alexa594 at sites corresponding to prominent vascular landmarks visible both in the in vivo two-photon imaging and under a dissecting scope during the ex vivo marking procedure. Confirmation of the imaging sites within the MEC was based on the presence of the lamina dissecans, the relative position of the post-rhinal border to the pin mark, and the characteristic circular shape of the dentate gyrus as observed in the medial-lateral sagittal sections. n = 6 mice. **b**. For each time cell, mean dF/F displayed for each trial type (top) and dF/F activity on each trial, sorted by trial type (below).

https://doi.org/10.1038/s41593-024-01683-7

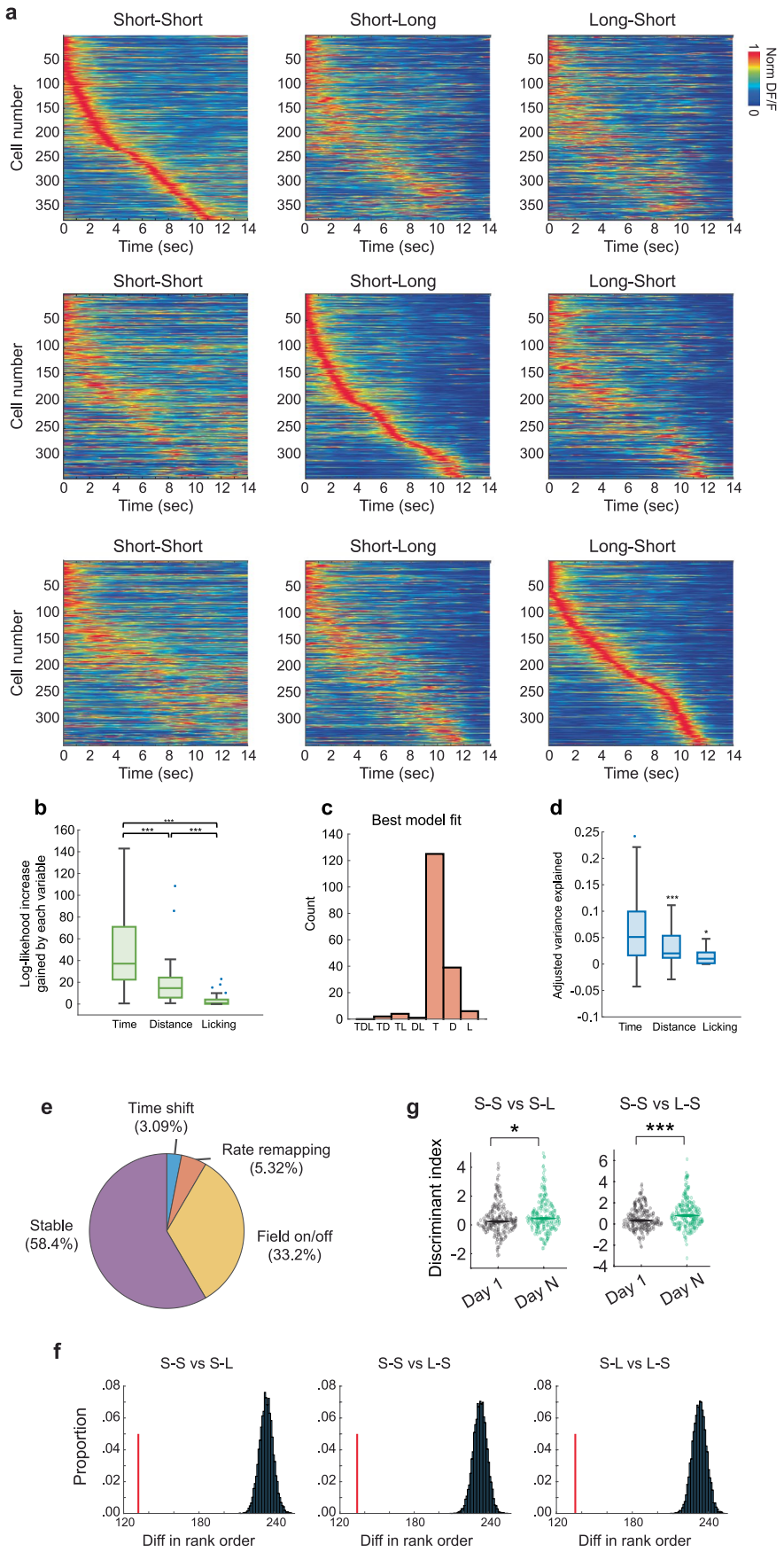

Extended Data Fig. 3 | See next page for caption.

https://doi.org/10.1038/s41593-024-01683-7

Extended Data Fig. 3 | Additional analysis on time cell tuning. a. Top, sequence of MEC time cells significantly tuned for S-S trials, sorted by S-S trials and displayed for S-S, S-L and L-S trials. Middle, same as above, expect for significant MEC time cells on S-L trials and sorted by S-L trials. Bottom, same as top, except for significant MEC time cells on L-S trials and sorted by L-S trials. **b**. A generalized linear model was used to assess whether neurons are tuned to one of three variables- time in the trial, distance travelled from trial start, or licking – or a combination of 2 or 3 variables (see Methods). Analysis performed on n = 695 time cells, collected from 10 behavioral sessions, lead to n = 177 significant models. Boxplot showing log-likelihood increase gained by each variable: time (median = 37.15), distance (median = 14.63) and licking (median = 0.82) (two-sided Kruskal-Wallis test, $p = 2.6\times10^{-26}$; followed by two-sided Wilcoxon rank-sum test with Bonferroni-correction: Time vs. Distance: $p = 1.7\times10^{-08}$; Time vs. Licking: $p = 3.7\times10^{-22}$; Distance vs. Licking: $p = 8.8\times10^{-13}$). Log-likelihood was normalized to recording time in minutes. **c**. Histogram demonstrating the model that best described the calcium activity of each cell and trial type. **d**. Boxplot showing adjusted variance explained for models that best describe the calcium activity of each cell for the single variable models: time (median = 0.0512), distance (median = 0.0202) and licking (median = 0.0101). Number of models n = 125,396. (One-sided Wilcoxon signed rank test (median greater than 0), p = 0.0001, p = 0, p = 0.0312). For box plots, the line inside of each box is the sample median. The upper quartile corresponds to the 0.75 quantile and the lower quartile corresponds to the 0.25 quantile. The blue dots in b and d represent outliers. Outliers are values that are more than 1.5 × interquartile range (IQR) away from the top or bottom of the box. The whiskers are lines that extend above and below each box. One whisker connects the upper quartile to the nonoutlier maximum (the maximum data value that is not an outlier), and the other connects the lower quartile to the nonoutlier minimum. **e**. Proportion of MEC time cells that either remained stable, displayed a time shift, displayed rate remapping, or displayed on/off dynamics across trial types. **f**. Rank order analysis for shuffle distribution (black) and real data (red). The similarity of the sequences of time cells across trial types is examined by comparing their rank orders. Each time cell is assigned three rank orders, corresponding to its sorting by peak timing for each trial type. Subsequently, the mean difference between rank orders within a cell is compared to a shuffle distribution, generated by shuffling rank order of cells 10,000 times. The p-value is computed as the proportion of shuffle values smaller than the actual data. Notably, p-values are zero for all three comparisons. **g**. Discriminant Index indicates the extent to which the difference in dF/F between trial types deviates from chance level. S-S vs S-L: Day 1 n = 224, Day N n = 221, z = 2.55, p = 0.01; S-S vs L-S: Day 1 n = 225, Day N n = 231, z = 3.80, $p = 1.4\times10^{-4}$, two-sided Wilcoxon rank sum test. Individual data points with median.

https://doi.org/10.1038/s41593-024-01683-7

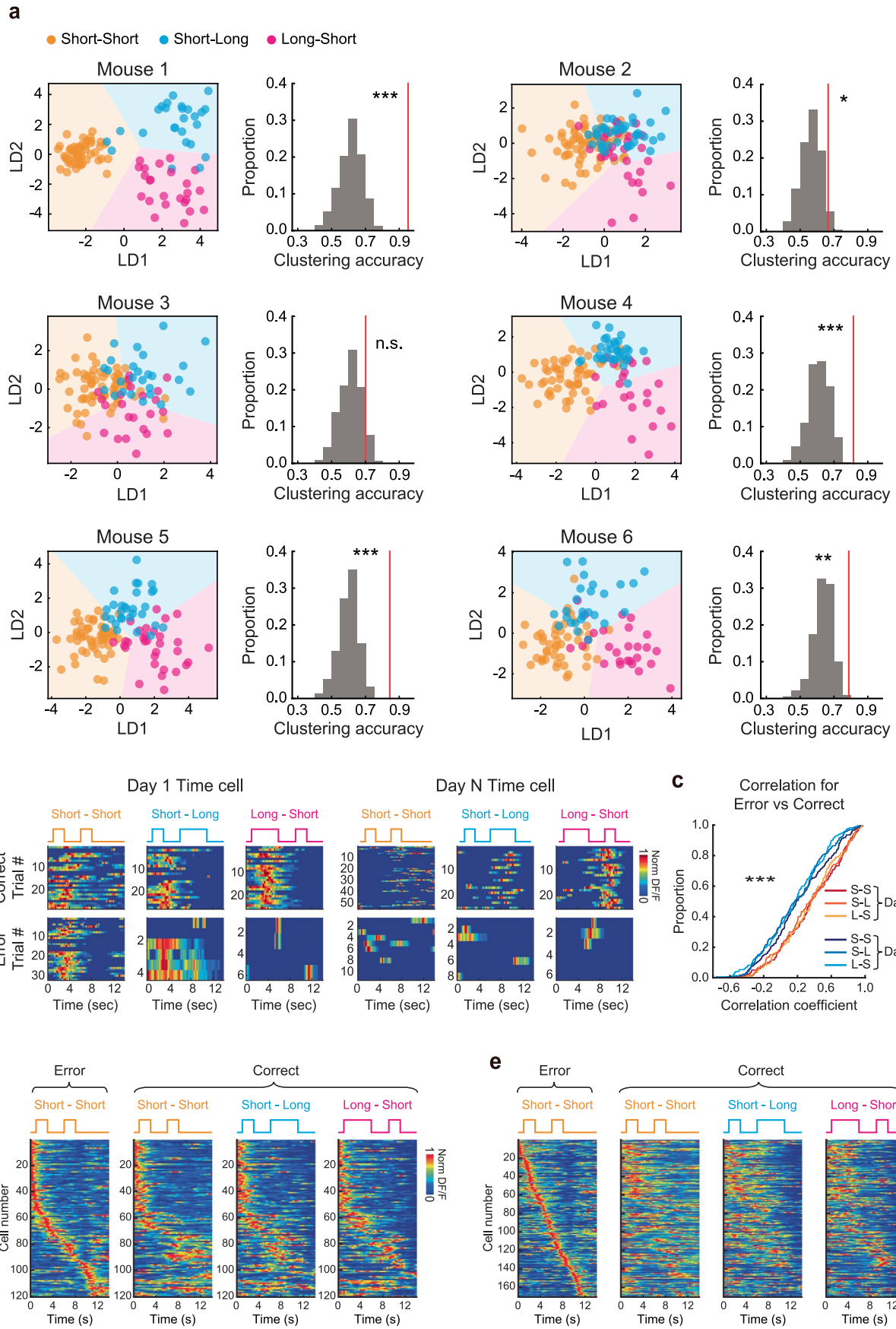

Extended Data Fig. 4 | See next page for caption.

https://doi.org/10.1038/s41593-024-01683-7

Extended Data Fig. 4 | Trial type decoding analysis for each mouse, and comparison of time cell activity on correct and error trials. a. For each panel: Left, LDA plots for each mouse on each trial type (S-S – orange, S-L – Blue, L-S – Magenta). K-means clustering is then applied to the LDA plots to categorize the dots into three clusters. The background colors indicate the clustering result. The accuracy of clustering analysis is determined by the proportion of dots correctly classified into their respective trial type. Right, clustering accuracy is compared between the bootstrapped shuffle distribution with randomly assigned trial labels (grey) and the actual data (red). The p-value is computed as the proportion of shuffle values larger than the actual data (one-sided). For mouse 1 through 6: p = 0, 0.04, 0.08, 0, 0, 0.001, respectively. No adjustment was made for multiple comparisons. **b**. Representative examples of MEC time cells on day 1 (left) and day N (right), depicting activity for both correct and error trials across all three types of trials. **c**. Cumulative distribution functions of correlation coefficients calculated for each MEC time cell, comparing activity across different trial conditions on day 1 and day N. session type main effect: $p = 2.3\times10^{-5}$, $F_{(1, 288)} = 18.5$; trial type main effect: $p = 0.12$, $F_{(1.93, 555.15)} = 2.1$; interaction: $p = 0.33$, $F_{(1.93, 555.15)} = 1.1$, two-way mixed ANOVA with trial type and session factors. **d**. Sequence of activity of MEC time cells recorded on day 1, arranged according to their activity during error trials on Short-Short (S-S) trials. This sequence is then applied to display cell activity for all three trial conditions during correct trials, maintaining the order from the error trials. **e**. Same as in d, but for recordings on day N.

https://doi.org/10.1038/s41593-024-01683-7

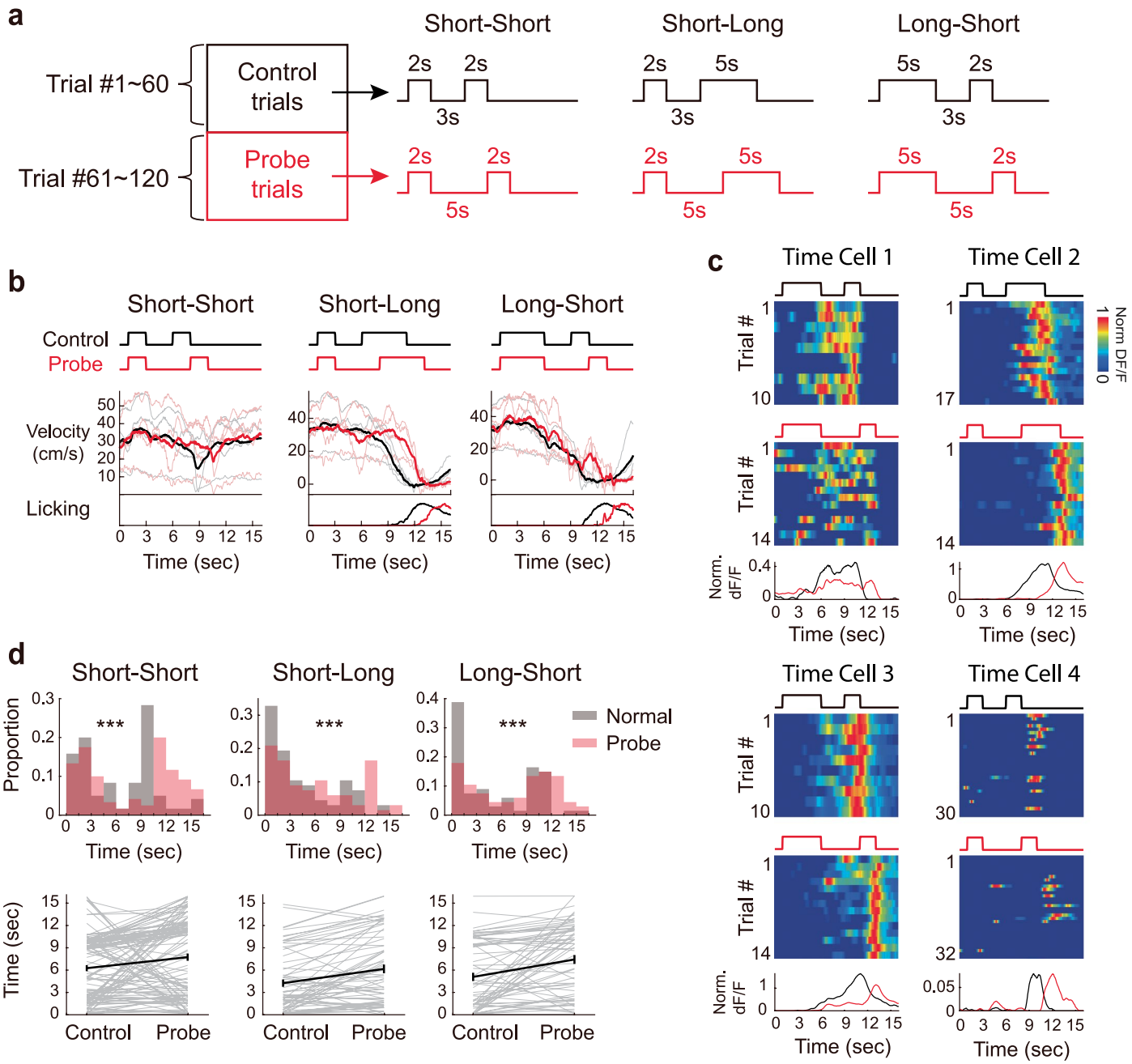

Extended Data Fig. 5 | MEC time cells on ISI probe trials. a. Schematic for probe trials. **b.** Comparative analysis of mean velocity and licking behaviors under three different conditions: Short-Short, Short-Long, and Long-Short, during standard (black) and probe (red) trials. **c.** Four example MEC time cells during control (black) and probe (red) trials. **d.** Aggregated data showing the timing of peak responses across the MEC time cell population under Short-Short, Short-Long, and Long-Short conditions, compared between standard (black) and probe (red) trials. Short-Short trial types: n = 120, p = 9.0×10^{-5}, z = 3.9; Short-Long trial types: n = 67, p = 7.4×10^{-6}, z = 4.5; Long-Short trial types: n = 67, p = 3.2×10^{-5}, z = 4.2, two-sided Wilcoxon signed-rank.

https://doi.org/10.1038/s41593-024-01683-7

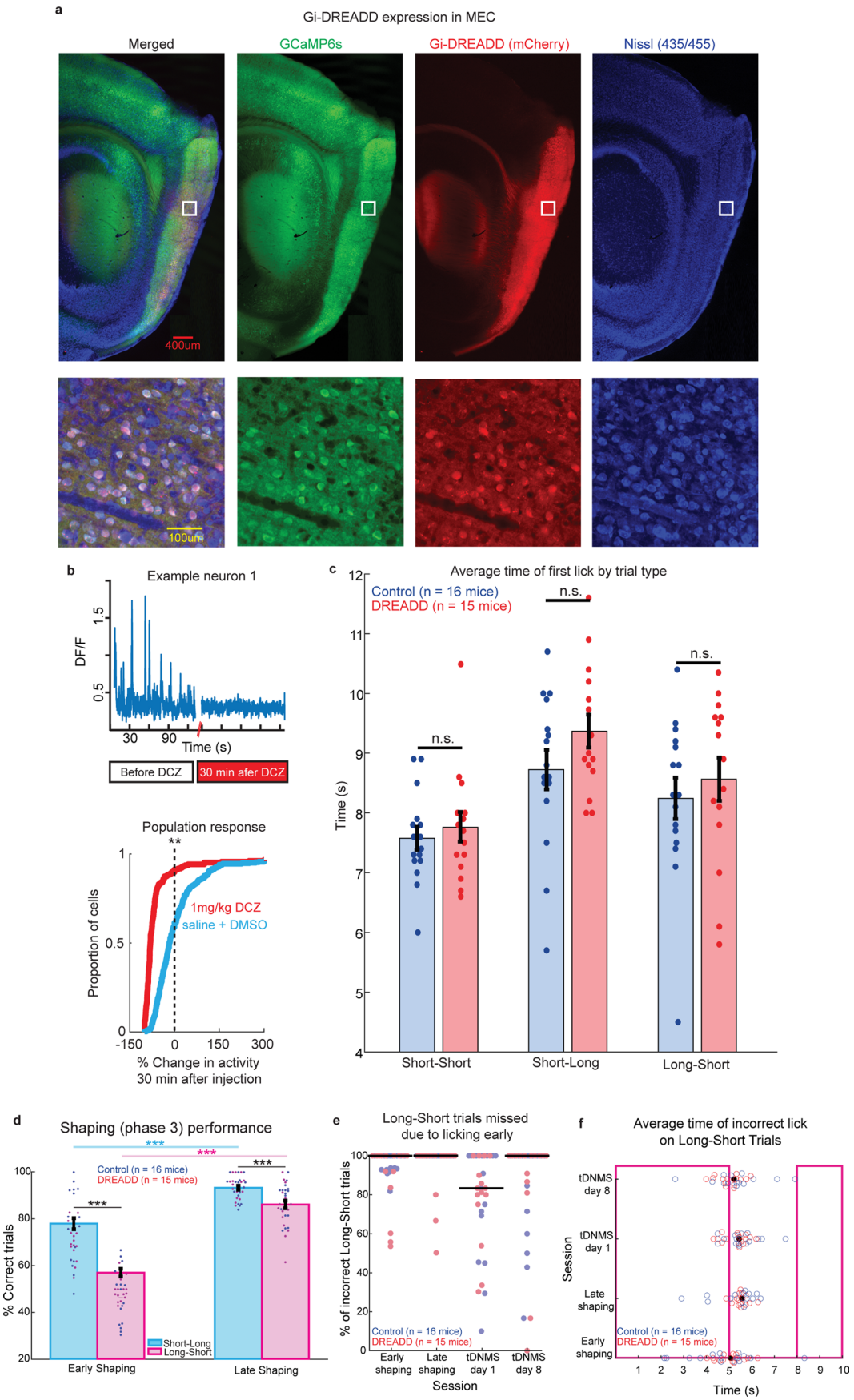

Extended Data Fig. 6 | See next page for caption.

https://doi.org/10.1038/s41593-024-01683-7

Extended Data Fig. 6 | MEC DREADD inactivation. a. Ability to inhibit MEC was confirmed using in-vivo 2-photon imaging combined with hM4D(Gi) inactivation. Histology showing co-expression of GCaMP6s and hM4D(Gi)-mCherry in MEC, one section from one mouse is shown**. b**. Activation of inhibitory DREADDs by 1 mg/kg I.P. injection of DCZ reduces average number of Ca2+ transients in MEC neurons by 80% at 30 minutes post injection compared to before DCZ injection. Top, example neuron before and after DCZ administration. Bottom, population response. In both the control (blue) and DCZ (red) conditions, GCaMP activity was monitored over 5-minute periods, and the change in activity was measured for each cell (n = 205 neurons in DCZ condition and n = 364 neurons in control condition, measured across two sessions in each condition; $p < 0.01$, two-tailed Kolmogorov-Smirnov test). **c**. Average time of first lick relative to first odor onset on session 1 of the tDNMS task for mice in Fig. 4. Dots show average time of first lick for each mouse, with bars showing mean ± s.e.m. across mice. There is no difference in average time of first lick for DREADD (n = 15) and Control (n = 16) mice in any trial type (Short-Short: $p = 0.56$, Short-Long: $p = 0.14$, Long-Short: $p = 0.52$, two-tailed unpaired t-tests). **d**. Average performance by trial type during shaping for mice in Fig. 4 (n = 31 mice). Shaping consists of probe trials where mice must correctly trigger reward and automatic trials where reward is automatically given. Performance was examined on all probe trials within the first 1/2 session of shaping phase 3, termed "early shaping", and the last 1/2 session of shaping phase 3, or "late shaping", for each mouse. Mice performed better on short-long trials than long-short both early ($p = 2.9 \times 10^{-8}$, two-tailed paired t-test) and late (8.5×10^{-4}, two-tailed paired t-test) in shaping. Additionally, performance was higher for both short-long ($p = 1.3 \times 10^{-8}$, two-tailed paired t-test) and long-short ($p = 3.1 \times 10^{-15}$, two-tailed paired t-test) trials in late compared to early shaping. Dots represent performance of each mouse, with blue dots for Control mice (n = 16) and red for DREADD mice (n = 15). Bars show mean ± s.e.m. across all mice. **e**. Reason for mistakes on long-short trials for mice in Fig. 4. During shaping phase 3 and the tDNMS task, mice can miss nonmatch trials either by withholding licking or by licking prematurely during the first odor and/or interstimulus interval. The percent of incorrect long-short trials missed due to licking early is shown. Dots indicate values for each mouse, with DREADD mice shown in red (n = 15) and Control in blue (n = 16), and black lines show the median value across all mice. **f**. Average time of first incorrect lick on long-short trials relative to first odor onset for mice in Fig. 4. Blue (Control, n = 16) and red (DREADD, n = 15) circles represent the average time of first lick on all incorrect long-short trials for a given mouse, and black dots show the median value across all mice.

https://doi.org/10.1038/s41593-024-01683-7

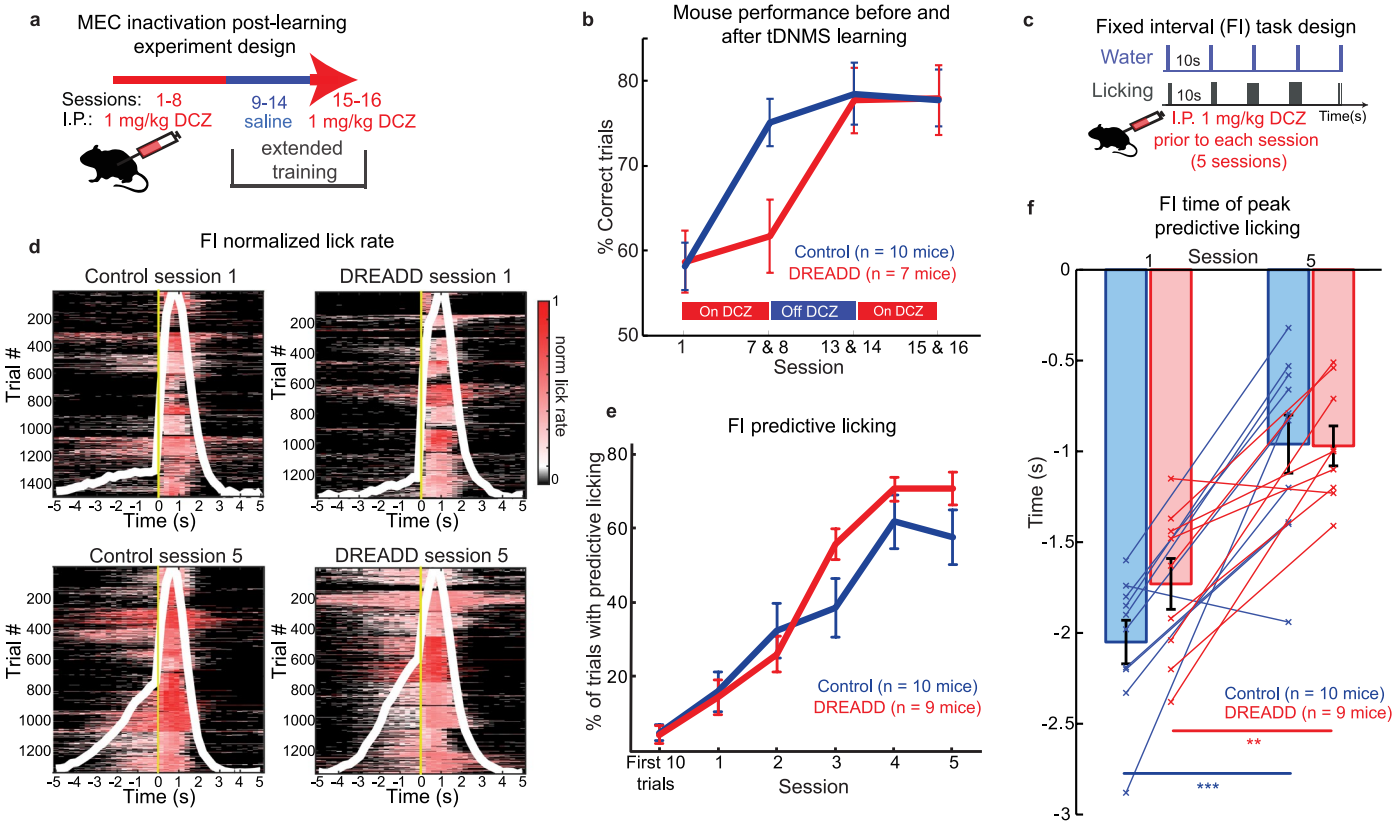

Extended Data Fig. 7 | MEC is not required for all interval timing behavior. **a**. Schematic for inhibiting MEC after learning in the tDNMS task. After experiments testing the role of MEC during learning (Fig. 4), a subset of mice (n = 7 DREADD, n = 10 Control) underwent extended training to determine whether MEC is necessary for ongoing task performance. **b**. Though MEC inhibition impaired learning in the tDNMS task (Sessions 1-8), DREADD mice learned the task in the absence of MEC inhibition (Sessions 9-14). Following learning, subsequent administration of DCZ to inactivate MEC did not affect performance in Sessions 15-16. Bars indicate mean performance ± s.e.m calculated across mice. **c**. Fixed interval task schematic. MEC DREADD (n = 9) and Control (n = 10) mice were trained on a fixed interval (FI) task (Toda et al. 2017). A droplet of water (4-6ul) was delivered every 10 s to head-fixed mice. Licking was measured; time-locked predictive licking indicates learning the timing of water delivery. The DREADD agonist DCZ (1 mg/kg) was delivered 5 min prior to each session. **d**. Licking behavior of DREADD (n = 9) and Control (n = 10) mice on sessions 1 and 5 of the FI task. Licking was normalized to the maximum lick frequency with each session for each mouse. All trials for all mice are shown; water delivery occurs at 0 s, indicated by a yellow line. Average lick response for each session is shown in white. **e**. Fixed interval learning. Predictive licking is defined as an increase in lick rate, measured over 5 seconds preceding the upcoming reward delivery. Both DREADD and Control mice learn the temporal structure of the task, as demonstrated though more frequent engagement in predictive licking from sessions 1-5. Data represent mean ± s.e.m. averaged across mice. **f**. Average time of peak predictive licking activity in FI task relative to upcoming water delivery. From session 1 to 5, peak predictive licking activity moves closer to reward delivery (0 s) for both Control ($p = 2.2 \times 10^{-4}$, two-tailed paired t-test) and DREADD mice ($p = 0.0013$ two-tailed paired t-test). Data points represent average time of peaking licking on Session 1 and 5 for each mouse; bars indicate mean ± s.e.m. across mice.

https://doi.org/10.1038/s41593-024-01683-7

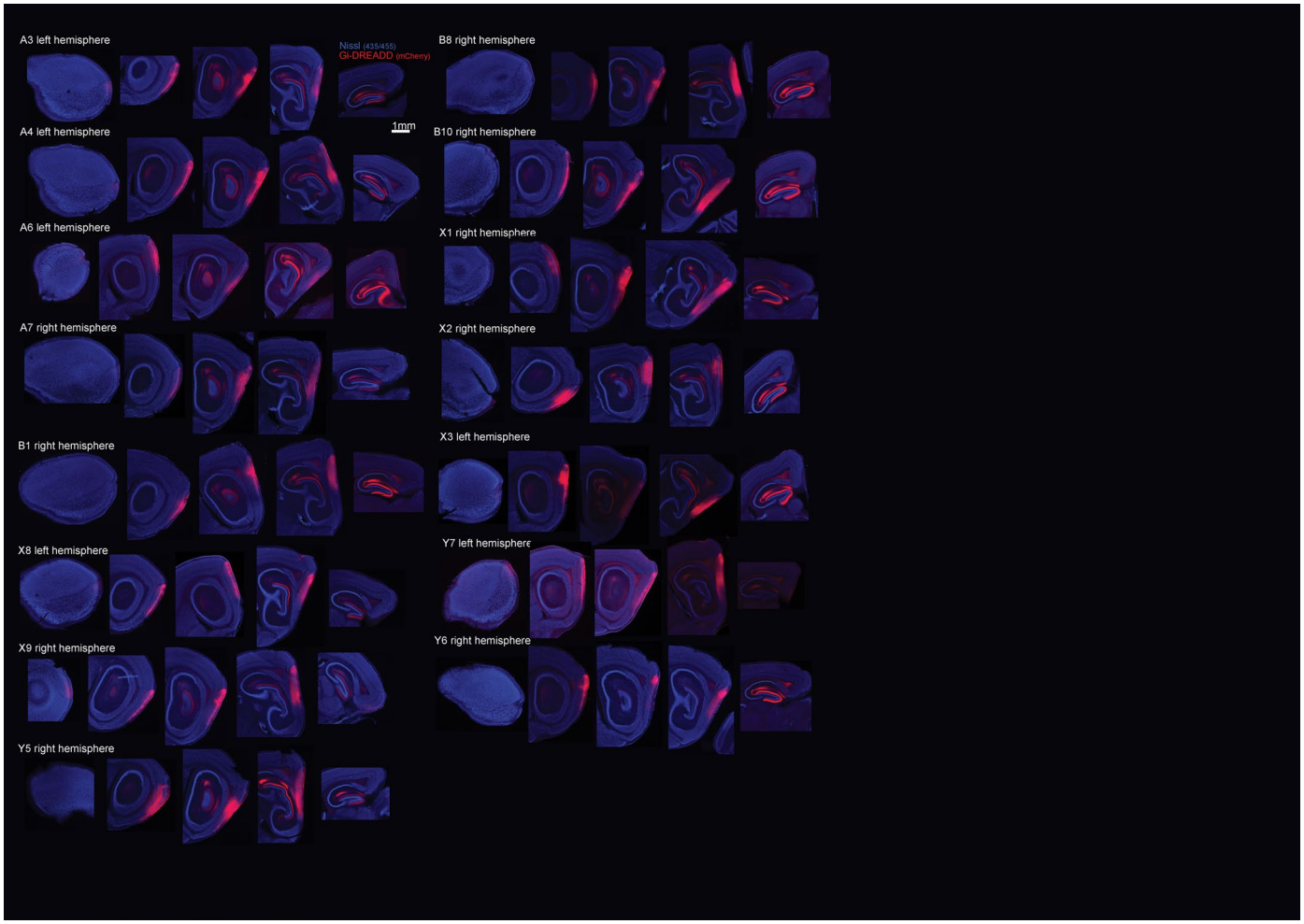

Extended Data Fig. 8 | Histology showing expression of hM4D(Gi)-mCherry in MEC. Injections were performed bilaterally; sections spanning one hemisphere are shown for each DREADD mouse from Fig. 4 (n = 15, mouse identity and hemisphere noted). Five sagittal sections are shown per mouse, ranging from lateral (left) to medial (right). The middle three sections include MEC.

https://doi.org/10.1038/s41593-024-01683-7

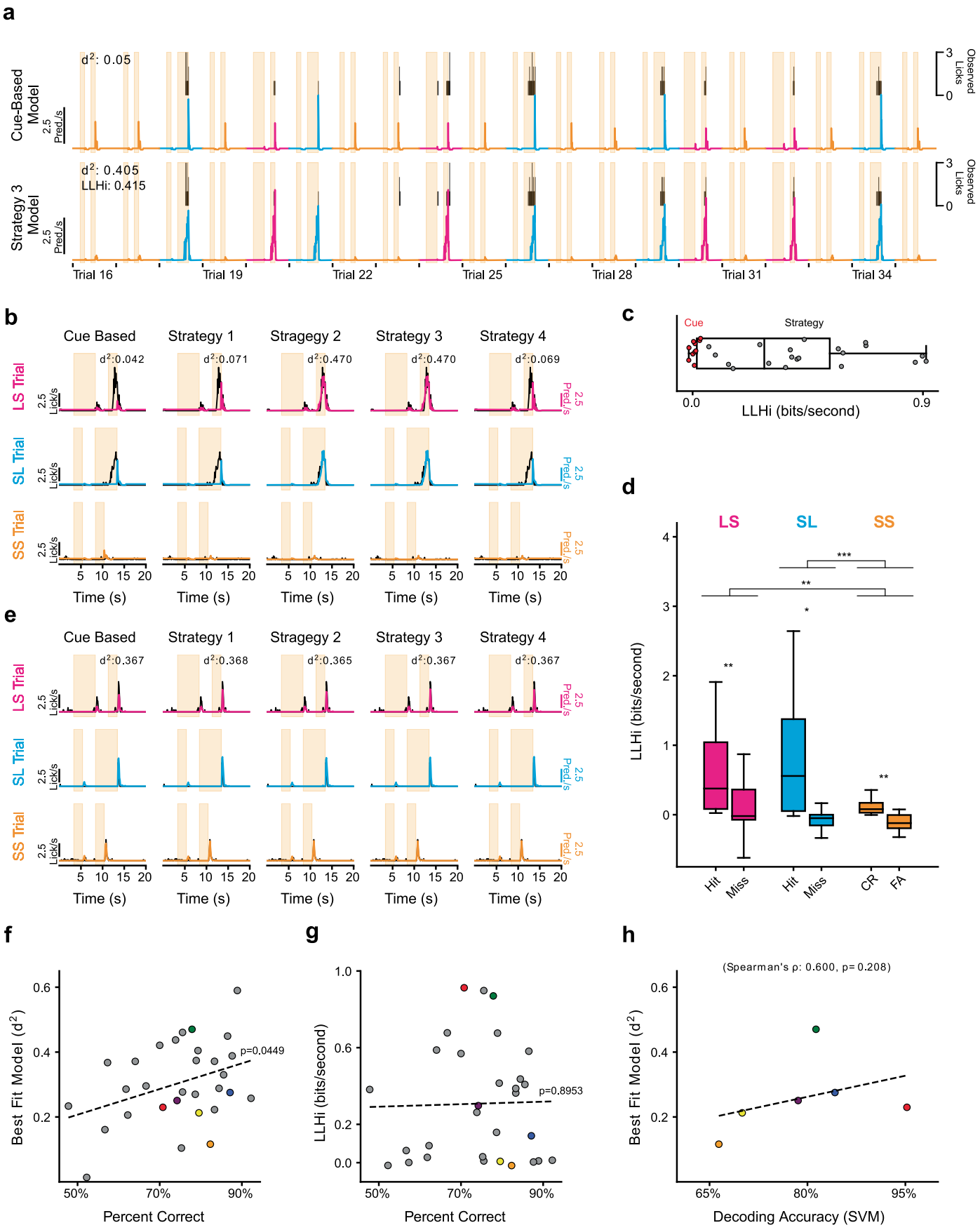

Extended Data Fig. 9 | See next page for caption.

https://doi.org/10.1038/s41593-024-01683-7

Extended Data Fig. 9 | Additional details on Poisson Regression analysis of behavior. a. Example of modeling behavior during tDMNS task. *Top*. Baseline cue-based model including only odor offset, long cue, and second cue features. *Bottom*. Strategy-based model. Observed anticipatory licks are in black above each model's predicted value. **b**. Comparison of cue-based and strategy-based models for an individual animal. Mean lick rate for each trial type in black, model predictions in color. **c**. Fitting a Gaussian Mixture Model with 2 components to the best fitting LLHi over the cue-based model reveals two populations: one cue-based where additional features do not improve model performance (n = 10 mice) and one strategy-based with improved model predictions (n = 20 mice). **d**. A strategy-based model fits better on hit/correct reject trials compared to miss/false alarm (based on Strategy 3) (n = 30 mice, two-factor ANOVA significant effect for trial type $F(2,155) = 7.64$, $p = 6.88\times10^{-4}$ and result $F(1,155) = 35.6$, $p = 1.58\times10^{-8}$, but not type x result $F(5,155) = 2.26$, $p = 0.11$, post-hoc tests: * - $p < 0.05$, ** - $p < 0.01$, *** - $p < 0.001$). **e**. Example cue and strategy-based models for an animal where both fit similarly. **f**. Relationship between average mouse performance on the task and how well models fit the data (linear regression, $r = 0.369$, $p = 0.045$). **g**. No significant relationship between average percent correct and evidence for animals using a strategy-based solution, based on best fitting strategy (linear regression, $r = 0.025$, $p = 0.895$). **h**. No significant relationship between ability to decode trial type from the neural data and the ability to fit a model to the behavior, based on best fitting strategy (strategy and cue-based models, $\rho = 0.600$, $p = 0.208$, two-sided Spearman's rank test for correlation and t-statistic). Colors in panels **f**-**h** indicate imaged mice, gray indicates not imaged. Center line on box plots depicts the median, the first and third quartiles are indicated by extent of the box and whiskers indicate the outlier cutoff (1.5x inter-quantile range).

https://doi.org/10.1038/s41593-024-01683-7

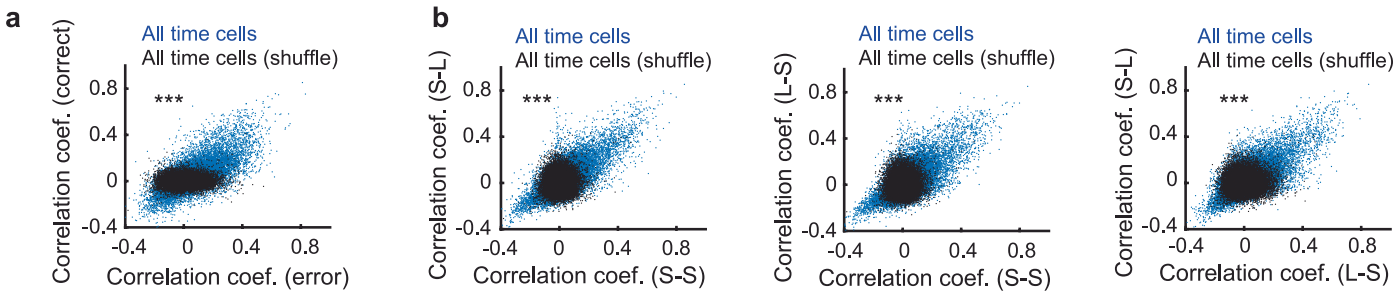

Extended Data Fig. 10 | Activity correlation between time cells maintained across conditions. a. Pairwise correlation between all time cells during correct trials and error trials in the tDNMS task shown for real (blue) and shuffled data (black). n = 15,727, z = 69.6, p = 0, two-sided Chi-squared test. **b.** Same as in a, but shown for correct trials on each trial type (S-S vs S-L, right; S-S vs L-S, middle; L-S vs S-L, right). S-S vs S-L: n = 15,727, z = 72.4, p = 0; S-S vs L-S: n = 15,727, z = 66.3, p = 0; L-S vs S-L: n = 15,727, z = 65.8, p = 0, two-sided Chi-squared test.

nature portfolio

Corresponding author(s): James G. Heys

Last updated by author(s): Apr 29, 2024

Reporting Summary

Nature Portfolio wishes to improve the reproducibility of the work that we publish. This form provides structure for consistency and transparency in reporting. For further information on Nature Portfolio policies, see our Editorial Policies and the Editorial Policy Checklist.

Statistics

For all statistical analyses, confirm that the following items are present in the figure legend, table legend, main text, or Methods section.

n/a	Confirmed	
☐	☒	The exact sample size (*n*) for each experimental group/condition, given as a discrete number and unit of measurement
☐	☒	A statement on whether measurements were taken from distinct samples or whether the same sample was measured repeatedly
☐	☒	The statistical test(s) used AND whether they are one- or two-sided *Only common tests should be described solely by name; describe more complex techniques in the Methods section.*
☒	☐	A description of all covariates tested
☐	☒	A description of any assumptions or corrections, such as tests of normality and adjustment for multiple comparisons
☐	☒	A full description of the statistical parameters including central tendency (e.g. means) or other basic estimates (e.g. regression coefficient) AND variation (e.g. standard deviation) or associated estimates of uncertainty (e.g. confidence intervals)
☐	☒	For null hypothesis testing, the test statistic (e.g. *F*, *t*, *r*) with confidence intervals, effect sizes, degrees of freedom and *P* value noted *Give P values as exact values whenever suitable.*
☒	☐	For Bayesian analysis, information on the choice of priors and Markov chain Monte Carlo settings
☒	☐	For hierarchical and complex designs, identification of the appropriate level for tests and full reporting of outcomes
☐	☒	Estimates of effect sizes (e.g. Cohen's *d*, Pearson's *r*), indicating how they were calculated

Our web collection on statistics for biologists contains articles on many of the points above.

Software and code

Policy information about availability of computer code

Data collection	All experimental paradigms were automated and controlled using an Ardunio Uno and custom code, and data collection was performed using a Picoscope oscilloscope (PICO4824, Pico Technology, v6.13.2). Imaging data were collected using a Neurolabware microscope and Scanbox Scanbox v4.1 software.
Data analysis	Imaging data was analyzed on a IBuyPower Intel Core with Windows10 using Suite2P v0.10.1 and custom software written in Matlab (2018b). Licking behavior was modeled using custom code in Python 3.11.4. All other analysis was performed with custom code written in Matlab (2018b). Code is available at https://github.com/heyslab/Bigus_Lee_NatNeuro_2024 or upon reasonable request to the corresponding author. A subset of experimental schematics shown in figures were made using BioRender.

For manuscripts utilizing custom algorithms or software that are central to the research but not yet described in published literature, software must be made available to editors and reviewers. We strongly encourage code deposition in a community repository (e.g. GitHub). See the Nature Portfolio guidelines for submitting code & software for further information.

Data

Policy information about availability of data

All manuscripts must include a data availability statement. This statement should provide the following information, where applicable:

- Accession codes, unique identifiers, or web links for publicly available datasets
- A description of any restrictions on data availability
- For clinical datasets or third party data, please ensure that the statement adheres to our policy

Data presented in this study are available upon reasonable request to the corresponding author and will be made publicly available at https://github.com/heyslab/Bigus_Lee_NatNeuro_2024 1.5 years after publication.

Research involving human participants, their data, or biological material

Policy information about studies with human participants or human data. See also policy information about sex, gender (identity/presentation), and sexual orientation and race, ethnicity and racism.

Reporting on sex and gender	N/A
Reporting on race, ethnicity, or other socially relevant groupings	N/A
Population characteristics	N/A
Recruitment	N/A
Ethics oversight	N/A

Note that full information on the approval of the study protocol must also be provided in the manuscript.

Field-specific reporting

Please select the one below that is the best fit for your research. If you are not sure, read the appropriate sections before making your selection.

☒ Life sciences ☐ Behavioural & social sciences ☐ Ecological, evolutionary & environmental sciences

For a reference copy of the document with all sections, see nature.com/documents/nr-reporting-summary-flat.pdf

Life sciences study design

All studies must disclose on these points even when the disclosure is negative.

Sample size	No statistical methods were used to predetermine sample sizes. Sample sizes were based on reliably measuring experimental parameters while remaining in compliance with ethical guidelines to minimize the number of animals used. Sample sizes were based on and comparable to prior work (Heys et al. 2020, Heys & Dombeck 2018, Toda et al. 2017).
Data exclusions	A subset of mice were removed from analysis for the tDNMS DREADD inactivation experiments due to: a failure to retain the task structure learned in shaping (performance >3 SD below the mean on tDNMS session 1, n =1 mouse), headplate falling off (n = 1 mouse), or lack of virus expression (n = 2 mice).
Replication	MEC inactivation experiments were performed in two cohorts of mice, with the second cohort successfully replicating the first. Imaging data were also reproducible, given consistent findings across 6 mice.
Randomization	Mice were randomly allocated into control and experimental conditions in the DREADD inactivation experiments; however, we ensured there were an equal number of males and females in each condition.
Blinding	The experimenter was blind to experimental condition for all training on the tDNMS task but was unblinded prior to the subsequent Fixed Interval experiment to permit tDNMS data analysis.

Reporting for specific materials, systems and methods

We require information from authors about some types of materials, experimental systems and methods used in many studies. Here, indicate whether each material, system or method listed is relevant to your study. If you are not sure if a list item applies to your research, read the appropriate section before selecting a response.

Materials & experimental systems

n/a	Involved in the study
☒	☐ Antibodies
☒	☐ Eukaryotic cell lines
☒	☐ Palaeontology and archaeology
☐	☒ Animals and other organisms
☒	☐ Clinical data
☒	☐ Dual use research of concern
☒	☐ Plants

Methods

n/a	Involved in the study
☒	☐ ChIP-seq
☒	☐ Flow cytometry
☒	☐ MRI-based neuroimaging

Animals and other research organisms

Policy information about studies involving animals; ARRIVE guidelines recommended for reporting animal research, and Sex and Gender in Research

Laboratory animals	C57-BL6 mice between 1.5-7 months in age were used for experiments. Wildtype C57-BL6 mice were used to establish the tDNMS task and for MEC inactivation experiments. Camk2a-tTA;tetO-GCaMP6s double transgenic heterozygotes were used for MEC imaging experiments.Mice were housed on a reversed 12h/12h light cycle, with a room temperature of approximately 21.1 degrees Celsius and humidity between 25-45%.
Wild animals	No wild animals were used.
Reporting on sex	MEC inactivation experiments were performed with equal numbers of male and female mice. No sex-dependent differences were found in preliminary experiments; therefore, sex-based analysis is not included in this manuscript. Both male and female mice were also used in imaging experiments.
Field-collected samples	No field-collected samples were used.
Ethics oversight	All experiments were approved and conducted in accordance with the University of Utah Animal Care and Use Committee.

Note that full information on the approval of the study protocol must also be provided in the manuscript.

Plants

Seed stocks	N/A
Novel plant genotypes	N/A
Authentication	N/A